



Impact of LHC vector boson production in heavy ion collisions on strange PDFs

A. Kusina^{1,a}, T. Ježo^{2,b}, D. B. Clark³, P. Duwentäster⁴, E. Godat³, T. J. Hobbs^{3,5}, J. Kent³, M. Klasen⁴, K. Kovařík^{4,c}, F. Lyonnet³, K. F. Muzakka⁴, F. I. Olness^{3,d}, I. Schienbein^{6,e}, J. Y. Yu⁶

¹ Institute of Nuclear Physics Polish Academy of Sciences, 31342 Kraków, Poland

² Institute for Theoretical Physics, KIT, Karlsruhe, Germany

³ Southern Methodist University, Dallas, TX 75275, USA

⁴ Institut für Theoretische Physik, Westfälische Wilhelms-Universität Münster, Wilhelm-Klemm-Straße 9, 48149 Münster, Germany

⁵ Jefferson Lab, EIC Center, Newport News, VA 23606, USA

⁶ Laboratoire de Physique Subatomique et de Cosmologie, Université Grenoble-Alpes, CNRS/IN2P3, 53 avenue des Martyrs, 38026 Grenoble, France

Received: 27 July 2020 / Accepted: 2 October 2020 / Published online: 19 October 2020

© The Author(s) 2020

Abstract The extraction of the strange quark parton distribution function (PDF) poses a long-standing puzzle. Measurements from neutrino-nucleus deep inelastic scattering (DIS) experiments suggest the strange quark is suppressed compared to the light sea quarks, while recent studies of W^\pm/Z boson production at the LHC imply a larger strange component at small x values. As the parton flavor determination in the proton depends on nuclear corrections, e.g. from heavy-target DIS, LHC heavy ion measurements can provide a distinct perspective to help clarify this situation. In this investigation we extend the nCTEQ15 nPDFs to study the impact of the LHC proton-lead W^\pm/Z production data on both the flavor differentiation and nuclear corrections. This complementary data set provides new insights on both the LHC W^\pm/Z proton analyses and the neutrino-nucleus DIS data. We identify these new nPDFs as **nCTEQ15WZ**. Our calculations are performed using a new implementation of the nCTEQ code (**nCTEQ++**) based on C++ which enables us to easily interface to external programs such as HOPPET, APPLgrid and MCFM. Our results indicate that, as suggested by the proton data, the small x nuclear strange sea appears larger than previously expected, even when the normalization of the W^\pm/Z data is accommodated in the fit. Extending the nCTEQ15 analysis to include LHC W^\pm/Z data represents an important step as we advance toward the next generation of nPDFs.

^a e-mail: aleksander.kusina@ifj.edu.pl

^b e-mail: tomas.jezo@kit.edu

^c e-mail: karol.kovarik@uni-muenster.de

^d e-mail: olness@smu.edu (corresponding author)

^e e-mail: ingo.schienbein@lpsc.in2p3.fr

Contents

1 Introduction	1
2 Fits to experimental data	3
3 Results and discussion	5
4 Comparisons	14
5 Conclusion	18
A Fitting data normalizations	19
References	19

1 Introduction

Parton distribution functions (PDFs) are key elements required to generate concrete predictions for processes with hadronic initial states in the context of QCD factorization theorems. The success of this theoretical framework has been extensively demonstrated in fixed-target and collider experiments (e.g., at the TeVatron, SLAC, HERA, RHIC, LHC), and will be essential for making predictions for future facilities (EIC, LHeC, FCC). Despite the above achievements, there is yet much to learn about the hadronic structure and the detailed composition of the PDFs [1, 4–20].

Although the up and down PDF flavors are generally well-determined across much of the partonic x range, there is significant uncertainty in the strange component, $s(x)$. The strange PDF is especially challenging because, in many processes, it is difficult to separate it from the larger down component. However, as we push to higher precision and energies, an accurate determination of the strange PDF is, apart from its intrinsic fundamental importance, essential not only for LHC measurements, but for a wide variety of pro-

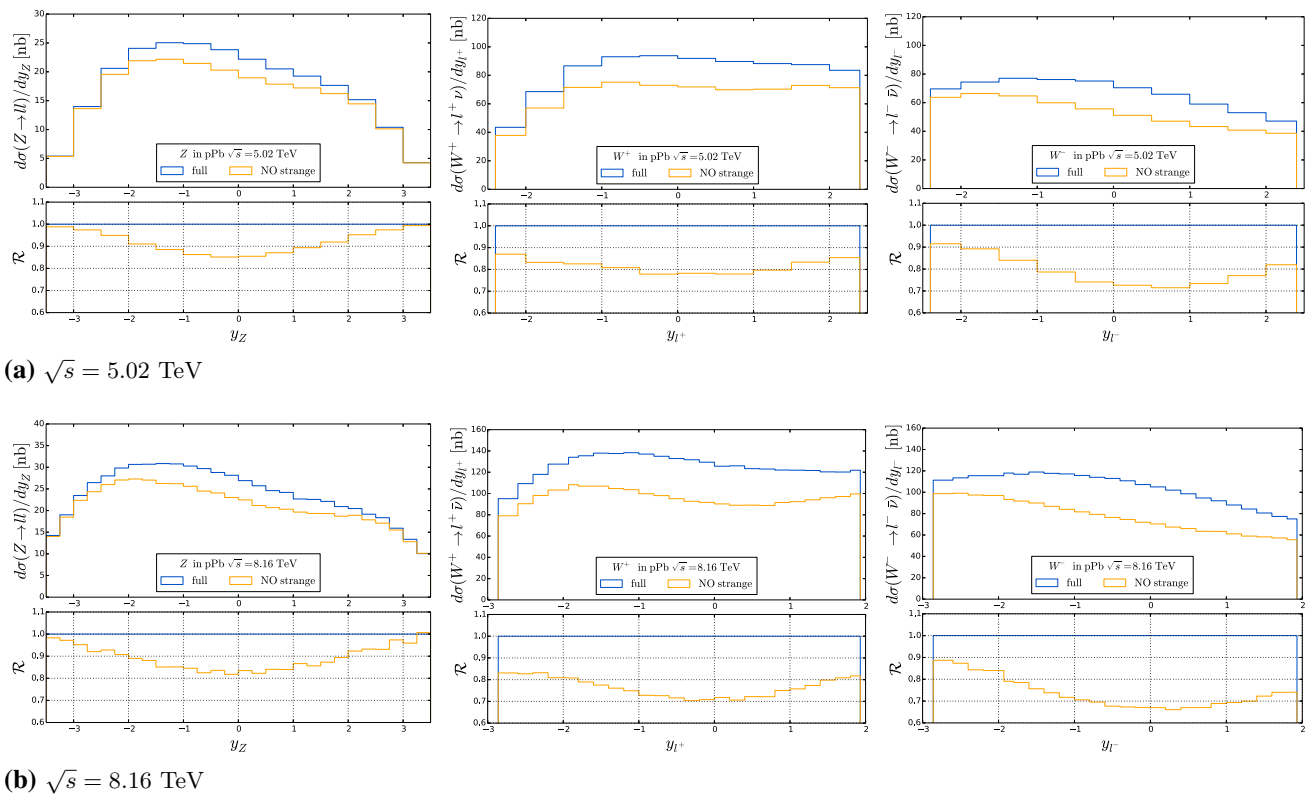


Fig. 1 Contribution of strange initiated channels to W^\pm and Z boson production for proton-lead (pPb) at the LHC. The blue lines represent total cross-sections, the yellow lines are cross-sections with the strange

initiated channels subtracted. The lower panels show the ratio compared to the total cross-section. This calculation used the nCTEQ15 nPDFs [1] with a modified version of the FEWZ [2,3] program

cesses [4, 13–20]. For example, the knowledge of the nuclear strange distribution in heavy nuclei is crucial for providing a reliable baseline for hard probes of the quark gluon plasma (QGP) which is characterized by enhanced production of strangeness [21–23]. Additionally, small x nuclear PDFs are essential for computing the composition of air showers from ultra-high energy cosmic rays [24–28].

The recent results from the LHC for inclusive W/Z boson production in pp collisions prefer a large strange to light-sea ratio [29–31]. This is a rather surprising result as it differs from earlier determinations based on analyses of neutrino deep inelastic scattering (DIS) data from NuTeV and CCFR experiments [32–34] or charged kaon production data from HERMES [35]. Furthermore, LHC measurements of associated $W + c$ production generally favor a smaller ratio for strange quark PDF, and this is more in line with the above fixed-target results. [36–38]. See Ref. [39] for more details on the earlier determinations of the strange distribution, and Ref. [40] for a study of the compatibility of the ATLAS and CMS results on associated $W + c$ and inclusive W/Z boson production using the xFitter framework [41].

It is not easy to directly compare the pp LHC results with the fixed target experiments, as the earlier measure-

ments were generally done using nuclear targets (typically Fe or Pb). Additional complications arise from the fact that there is a controversy about the proper nuclear correction factors for the charged current (CC) and neutral current (NC) DIS measurements [42–46]. As a result, the choice of heavy target neutrino DIS data sets varies widely among not just the many nuclear PDF (nPDF) determinations, but also for the proton PDF fits [4, 5]. Moreover, in the proton case the nuclear corrections are applied in different ways.

Conversely, it was already demonstrated that the W/Z LHC data can provide some important information on the strange and gluon nPDFs [6, 8, 47]. To demonstrate the impact of the heavy ion W^\pm/Z data on the strange PDF, in Fig. 1 we display the contribution of the strange-initiated process as a function of rapidity. We observe the strange component can be as much as 20–30% of the total. These plots were produced with FEWZ [2, 3] modified for the pPb beams using the nCTEQ15 nPDFs [1]. Since the nCTEQ15 nPDFs are based on a proton where the strange PDFs is given by $s + \bar{s} = \kappa(\bar{u} + \bar{d})$, we expect these plots to represent a conservative estimate of the strange contribution to the W/Z channels.

For this reason, we concentrate in the following on the constraints for the nuclear strange and gluon distributions given by the W and Z data from proton-lead ($p\text{Pb}$) collisions at the LHC. This process is an ideal QCD “laboratory” as it is sensitive to (i) the heavy flavor components $\{s, c, \dots\}$, (ii) the nuclear corrections, and (iii) the underlying “base” proton PDFs. Such an analysis provides an independent perspective on the subject and can help disentangle the flavor separation and nuclear modifications.

In the current investigation, we will study the production of W and Z bosons in proton–lead ($p\text{Pb}$) collisions at the LHC; this involves similar considerations as the pp case, but also brings in the nuclear corrections. We will be focusing, in particular, on the strange and gluon distributions to see how these are modified when the LHC measurements are included. In Sect. 2 we review the various data sets used in our analysis along with the separate fits extracted. In Sect. 3 we present the quality of the fits and comparisons of data with the theory, and demonstrate the impact on the resulting PDFs. In Sect. 4 we compare our final PDF fit with other results from the literature. In Sect. 5 we recap the key outcomes of this study. Finally, in Appendix A we provide additional details on the normalization of data sets and this contribution to the χ^2 .

2 Fits to experimental data

2.1 The nCTEQ++ framework

The nCTEQ project extends the proton PDF global fitting effort by fully including the nuclear dimension.¹ Previous to the nCTEQ effort, nuclear data was “corrected” to isoscalar data and added to the proton PDF fit *without* any uncertainties [48]. In contrast, the nCTEQ framework allows full communication between the nuclear data and the proton data; this enables us to investigate if observed tensions between data sets could potentially be attributed to the nuclear corrections.

The details of the nCTEQ15 nPDFs are presented in Ref. [1]. The present analysis is performed in a new C++ code base (**nCTEQ++**) which enabled us to easily interface to external programs such as HOPPET [49], APPLgrid [50], and MCFM [51]. The nCTEQ15 fit has been reproduced in this new nCTEQ++ framework.

For the current set of fits, we use the same 16 free parameters as for the nCTEQ15 set, and additionally open up three parameters for the strange PDF, for a total of 19 parameters. Recall that for the nCTEQ15 set, the strange PDF was constrained by the relation $s = \bar{s} = (\kappa/2)(\bar{u} + \bar{d})$ at the initial

scale $Q_0 = 1.3$ GeV so that it had the same form as the sea quarks.

Our PDFs are parameterized as

$$x f_i^{p/A}(x, Q_0) = c_0 x^{c_1} (1-x)^{c_2} e^{c_3 x} (1 + e^{c_4 x})^{c_5}, \quad (1)$$

and the nuclear A dependence is encoded in the coefficients as

$$c_k \longrightarrow c_k(A) \equiv c_{k,0} + c_{k,1}(1 - A^{-c_{k,2}}), \quad (2)$$

where $k = \{1, \dots, 5\}$.

The 16 free parameters used for the nCTEQ15 set model the x -dependence of the $\{g, u_v, d_v, \bar{d} + \bar{u}\}$ PDF combinations, and we do not vary the \bar{d}/\bar{u} parameters; see Ref. [1] for details. To this, we now add three strange PDF parameters: $\{c_{0,1}^{s+\bar{s}}, c_{1,1}^{s+\bar{s}}, c_{2,1}^{s+\bar{s}}\}$; these parameters describe, correspondingly, the overall normalization, the low- x exponent and the large x exponent of the strange distribution.

2.2 Experimental data sets

In this analysis we use the deep inelastic scattering (DIS), Drell–Yan (DY) lepton pair production, and RHIC pion data employed in our earlier nCTEQ15 analysis [1]. Additionally, we use W and Z inclusive data from proton-lead collisions at the LHC. Specifically, we include the following data sets: ALICE W^\pm boson production [57,58], ATLAS Z boson production [53], ATLAS W^\pm boson production [52], CMS Z boson production [55], CMS W^\pm boson production [54], CMS Run II W^\pm boson production [56], and LHCb Z boson production [59]. The data sets are outlined in Table 1. We note that ALICE has just released a new analysis of Z boson production in Ref. [60]; this data will be included in a future update.

For the calculation of the W^\pm/Z cross sections, we used the MCFM-6.8 program [61] to generate APPLgrid [50] tables which allow for efficient computation inside the Minuit fitting loop. As a cross check, we validate these grids using the FEWZ program [2,3] which has been modified to accommodate the proton-lead initial state. Similarly, we use a version of HOPPET [49], for our DGLAP evolution which is extended to accommodate grids of multiple nuclei.

All the theory calculations and PDF evolution are performed at the next-to-leading order (NLO) of QCD. Although the above tools allow for higher precision with NNLO calculations [62], the current uncertainties on the nuclear PDFs are sufficiently large that NLO accuracy is entirely satisfactory for our present study.

For the W^\pm/Z cross sections, our grids are also computed to NLO, and it is important to estimate the potential uncertainty arising from this choice. These cross sections have been computed out to NNLO in Ref. [63], and they observed a large shift between the LO and NLO results. However,

¹ For details, see <https://www.ncteq.org> which is hosted at [HepForge.org](https://hepforge.org).

Table 1 The overview of the LHC W^\pm/Z data sets including the $p\text{Pb}$ system with per nucleon center-of-mass energy $\sqrt{s_{NN}}$, experimental normalization uncertainty of the data σ_{norm} arising from the luminosity uncertainty, number of data points, and references

Data overview			$\sqrt{s_{NN}}$ [TeV]	σ_{norm} (%)	No points	References
ATLAS	Run I	W^\pm	5.02	2.7	10+10	[52]
ATLAS	Run I	Z	5.02	2.7	14	[53]
CMS	Run I	W^\pm	5.02	3.5	10+10	[54]
CMS	Run I	Z	5.02	3.5	12	[55]
CMS	Run II	W^\pm	8.16	3.5	24+24	[56]
ALICE	Run I	W^\pm	5.02	2.0	2+2	[57,58]
LHCb	Run I	Z	5.02	2.0	2	[59]

comparing the NLO and NNLO results for both W^\pm/Z production, they find the uncertainty bands are decreased but the NNLO results lie within the NLO error band. In a separate analysis, Ref. [64] computed the W^\pm/Z production cross sections in a PDF framework for both NLO and NNLO for both the Tevatron ($p\bar{p}$) and the LHC (pp). This study found the variation of the W^\pm/Z production cross sections in both cases to be about 1.5%, *c.f.*, Tables 1 and 2 of Ref. [64]. While we have not assigned any theoretical uncertainties in our current analysis, the above suggest a reasonable estimate would be on the order of a percent or two, and is small enough that it will not significantly alter our general conclusions. Similarly, the impact of the NNLO corrections to the DIS structure functions will be very small and even further minimized due to the fact that these data come as structure function ratios.

2.3 The PDF fits

We now use the **nCTEQ++** framework to include the LHC W^\pm/Z $p\text{Pb}$ data and extend the nCTEQ15 fit. Comparing the LHC $p\text{Pb}$ data to the nCTEQ15 results, we find that these data generally lie above the theory predictions [47]; hence, including a normalization uncertainty is essential to obtain a good fit to these data sets.

Normalization Factors: In our fits, we can allow for a floating normalization of individual data sets, and we label these N_{norm} as listed in Table 2. The experiments have an associated luminosity uncertainty, which we identify in Table 1 as σ_{norm} . As our fit modifies the floating normalizations factors N_{norm} , the quoted experimental luminosity uncertainties σ_{norm} serve as a gauge to calibrate these normalization shifts, and this contribution to the χ^2 computation is displayed in Table 3. Additional details are presented in Appendix A.

It is reasonable to tie the normalizations for data from individual experiments to a single normalization factor as these uncertainties are fully correlated. Thus, in our collection of fits below, we use a total of 3 normalization factors N_{norm} as summarized in Table 2: (1) ATLAS Run I $\{W^\pm, Z\}$, (2) CMS Run I $\{W^\pm, Z\}$, and (3) CMS Run II $\{W^\pm\}$. We do not add additional normalization factors for ALICE and LHCb sets as

they have limited data points and we obtain a good χ^2/N_{dof} without any normalization shift.

The Fits: Previous studies implied a close connection between the normalization of the W^\pm/Z data and the extracted strange PDF [47]. To systematically investigate the effect of the normalization in detail, we will use a series of fits outlined in Table 3 and summarized below:

nCTEQ15 This is the original set of nuclear PDFs as computed in Ref. [1].

Norm0 We include the LHC $p\text{Pb}$ data, but we do not allow for any floating normalization of the LHC data.

Norm2 We include the LHC $p\text{Pb}$ data, and allow for 2 normalization factors; one for the ATLAS Run I data, one for CMS Run I; we do not normalize CMS Run II data in this fit.

Norm3 We include the LHC $p\text{Pb}$ data, and we allow for 3 normalization factors; one for the ATLAS Run I data, one for the CMS Run I data, and a separate one for the CMS Run II data.

nCTEQ15WZ This is the same as Norm3, but we also include the RHIC inclusive pion data directly in the fit. This is discussed in Sect. 4.

All four of these new PDF fits are based on the DIS and DY data from the nCTEQ15 analysis and the LHC data sets, as outlined in Sect. 2.2 and Table 1.

As with our nCTEQ15 study, we will present results both with and without the inclusive pion data [65,66]. For the comparison of the the W^\pm/Z normalizations fits {Norm0, Norm2, Norm3}, we will not include the pion data; however, we do compute the pion χ^2 , as shown in Table 3, to demonstrate the compatibility.²

In Sect. 4 we then present a separate fit, nCTEQ15WZ, which does include the pion data. As we will see the impact of the pion data is marginal.

² Note that nCTEQ15WZ extends nCTEQ15 by adding the LHC W^\pm/Z data. In a similar manner, Norm3 extends the nCTEQ15np fit; however, we choose not to label this as nCTEQ15WZnp to avoid possible confusion.

Table 2 The LHC W^\pm/Z data sets and the corresponding ID's are listed. The applied normalization shifts N_{norm} (where appropriate) are applied to the data sets. The normalization shifts for the nCTEQ15WZ set are the same as for the Norm3 fit

Set ID	ATLAS Run I			CMS Run I			CMS Run II	
	W^-	W^+	Z	W^-	W^+	Z	W^-	W^+
	6211	6213	6215	6231	6233	6235	6232	6234
Normalization shifts: N_{norm}								
Norm 0	–			–			–	
Norm 2	0.963			0.949			–	
Norm 3	0.955			0.937			0.960	

The Normalization Shifts Table 2 shows the determined normalization factors N_{norm} used in each fit. All the normalization shifts are between 1σ and 2σ of the quoted normalization uncertainty σ_{norm} , but all are systematically below unity.

The appropriate normalization penalties are included in the χ^2 calculations, and the detailed prescription we use for fitting data normalizations is provided in Appendix A. In the case where no normalization shift is applied, we effectively have $N_{norm} = 1$, and the χ^2 contribution of the normalization shift is zero; *c.f.*, the last term of Eq. (6).

3 Results and discussion

Having presented our series of fits, we now examine (i) the quality of these fits as measured by the χ^2 values, (ii) the comparison of the data with our theory predictions, and (iii) the impact on the underlying PDFs.

3.1 Quality of the fits

Overall quality of the fits: In Table 3 we present the χ^2/N_{dof} for selected data sets as well as for each experiment type,³ and the contribution of the normalization penalty to the total χ^2/N_{dof} . We compute the normalization penalty as outlined in Appendix A, and this is included in the total.

Examining the total χ^2/N_{dof} of the fits, we see a broad range spanning from 1.66 for nCTEQ15 to values below 1.00, and an even larger range of the χ^2/N_{dof} for the individual LHC data sets.

Quality of individual data sets: To provide more details regarding the source of the χ^2 contributions, in Fig. 2 we display the χ^2/N_{dof} values for each individual experiment which enters the fit. The experiments are identified by their 4-digit ID, and the number of data points is indicated at the

top of each bar.⁴ Additionally, the bars are color-coded to indicate the type of observable {DIS, DY, W/Z}.

The χ^2/N_{dof} bar charts provide incisive information as to which data sets are driving the fit. We discuss each fit in turn.

nCTEQ15: Starting with the nCTEQ15 set, we note that (except for a few outliers) the DIS and DY data is well described by these PDFs;⁵ by comparison, the LHC W^\pm/Z data (which was **not** included in the original nCTEQ15 fit) is not well described. As was detailed in Ref. [47], an important contribution to this large χ^2 comes from the small x region where the nuclear PDFs are poorly constrained. The re-weighting analysis of Ref. [47] demonstrated that we can improve the fit by adjusting the small x behavior of the PDFs, but this alone will not bring all the data sets into the range of $\chi^2/N_{dof} \sim 1$; something else is required.

Norm0: As a first step, this fit includes the LHC W^\pm/Z data, but does not include any floating normalization factors. This fit will tell us the extent to which we can adjust the PDFs to fit the LHC data before we begin to adjust the normalization factors. Examining Fig. 2, we see the impact of the DIS and DY data on this fit is generally small for many of the data sets, but does result in noticeable improvement for a few of the sets including 5115 (NMC Ca/D) and 5121 (NMC Li/D), for example. However, it does significantly improve the LHC W^\pm/Z fit reducing the partial χ^2/N_{dof} of this data from 6.20 to 1.47 for the 120 LHC data points. Although this is a notable improvement, a number of the LHC data sets still have χ^2/N_{dof} values well above one.

Norm2: In this fit, we allow two floating normalization factors (one for ATLAS and one for CMS Run I) which are allowed to vary in the fit. The contribution of the normalization penalty is included in the total χ^2 .

We see the impact of the floating normalization factors on the DIS and DY data is again small, as was the case for the Norm0 fit. But the Norm2 fit dramatically improves the

³ When we refer to N_{dof} for the total χ^2 we calculate it in the usual way as the difference between number of data points and number of free parameters ($N_{dof} = N_{data} - N_{par}$). However, when referring to N_{dof} for individual experiments or data sets we set it to be equal to the number of data points ($N_{dof} = N_{data}$).

⁴ The IDs of the specific non-LHC experiments can be found in Ref. [1]. In general, DIS data sets are 51xx, DY sets are 52xx, and W^\pm/Z sets are 62xx.

⁵ We find the DIS experiments 5108 (Sn/D EMC-1988) and 5121 (Ca/D NMC-1995) to be outliers with $\chi^2/N_{dof} > 2$; this is consistent with other analyses [6,67].

Table 3 We present the χ^2/N_{dof} for the individual data sets, the individual processes {DIS, DY, Pion, LHC}, and the total. We also show the total χ^2 contribution from the LHC normalization penalty. Note that the Pion χ^2/N_{dof} is shown for comparison, but this data is only included in the nCTEQ15WZ fit

	ATLAS Run I		CMS Run I		CMS Run II		ALICE		LHCb	DIS	DY	Pion	LHC	LHC Norm χ^2	Total		
	W^-	W^+	W^-	W^+	W^-	W^+	W^-	W^+								Z	Z
χ^2/N_{dof} for selected experiments and processes																	
nCTEQ15	1.38	0.71	2.88	6.13	6.38	0.05	9.65	13.20	2.30	1.46	0.70	0.91	0.73	0.25	6.20	-	1.66
Norm0	0.94	0.26	2.71	3.89	2.25	0.03	1.07	1.51	0.53	0.02	0.71	0.92	0.95	[0.83]	1.47	-	1.03
Norm2	0.78	0.37	1.90	1.60	1.02	0.21	1.25	1.59	0.59	0.02	0.68	0.93	0.87	[0.61]	1.15	13.2	0.98
Norm3	0.83	0.46	1.78	1.41	1.23	0.31	0.74	0.84	0.75	0.08	0.62	0.90	0.77	[0.39]	0.91	22.9	0.91
nCTEQ15WZ	0.84	0.46	1.79	1.43	1.22	0.31	0.72	0.80	0.80	0.11	0.62	0.90	0.78	0.38	0.90	22.9	0.91

LHC W^\pm/Z data reducing χ^2/N_{dof} of this data to 1.15 as compared to 1.47 for the Norm0 fit. While the Norm2 fit is a substantial improvement over the Norm0 results and all LHC data sets have $\chi^2/N_{dof} < 2$, there are still a few sets at the upper limit of this range.

Norm3: Finally, we now perform a fit with three normalization factors: one for ATLAS (Run I), and one for each CMS Run I and CMS Run II.

As before, the modifications to the DIS and DY sets are minimal, but we do continue to see an improvement in the LHC sets; namely the χ^2/N_{dof} of this data improves to 0.91 as compared to 1.15 for the Norm2 fit.

Comparing Norm3 with nCTEQ15 for the other data sets, we see that the χ^2/N_{dof} for the DIS data is essentially the same (0.91 vs. 0.90), the DY increases slightly (0.73 vs. 0.77), and the pion χ^2 (computed a posteriori) increases slightly as well (0.25 vs. 0.39); these differences are relatively small compared to the significant improvement in the LHC data (6.20 vs. 0.90).

3.2 Comparison of data with theory

To obtain a more complete view of the fit quality, in Figs. 3, 4, 5, and 6 we display the comparison of the LHC data with theory predictions. The data points and errors are taken directly from the experimental measurements. However, it is important to note that we have shifted the theoretical predictions by the appropriate normalization factors; this allows us to present the fits with different normalizations on a single plot, and provides a more accurate visual description of the quality of the fit.

3.2.1 Large x region

Our first observation is that the experimental data consistently lies above our theoretical predictions. From Table 2, recall that **all** the fitted normalization factors are less than one, indicating that the fit prefers a reduction of the data values, typically in the range of $\sim 5\%$; because we have shifted the theory, this is not as obvious in Figs. 3, 4, 5 and 6.

Even with the normalization shifts, we see the theory predictions still lie well below the data for a number of sets. This is most evident in the negative y region for the Run I W^- data sets 6211 (ATLAS W^-) and 6231 (CMS W^- Run I), and to a lesser extent 6215 (ATLAS Z). Interestingly, the Run II data generally show good agreement across the full y range.

The negative rapidity region corresponds to the large x region of the lead PDF. The large x region is already rather well constrained by the fixed-target measurements, so there are limits as to how much the new LHC data can shift the PDFs in this region. Also note, that in the large x region we are in the “anti-shadowing region” ($x \sim 0.1$) where the nuclear corrections typically enhance the nuclear PDF relative to the

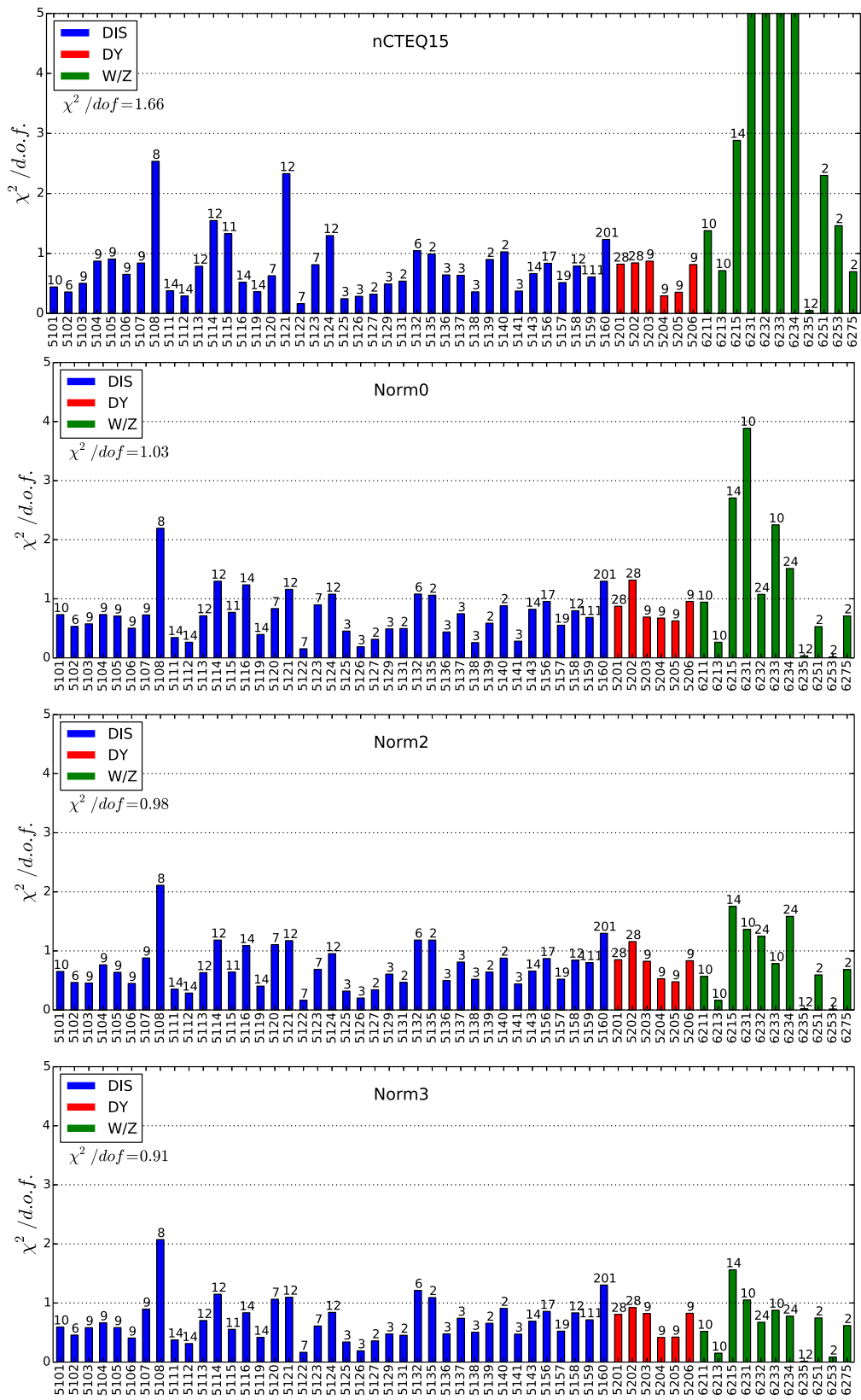


Fig. 2 The χ^2/N_{dof} of the individual experiments. The number of data points is indicated at the top of the bar, and the total χ^2/N_{dof} for the entire set is shown below the legend. For the nCTEQ15 set,

four of the bars extend beyond the chart range; these are $\chi^2/N_{dof} = \{6.1, 9.7, 6.4, 13.2\}$ for experiments $\{6231, 6232, 6233, 6234\}$

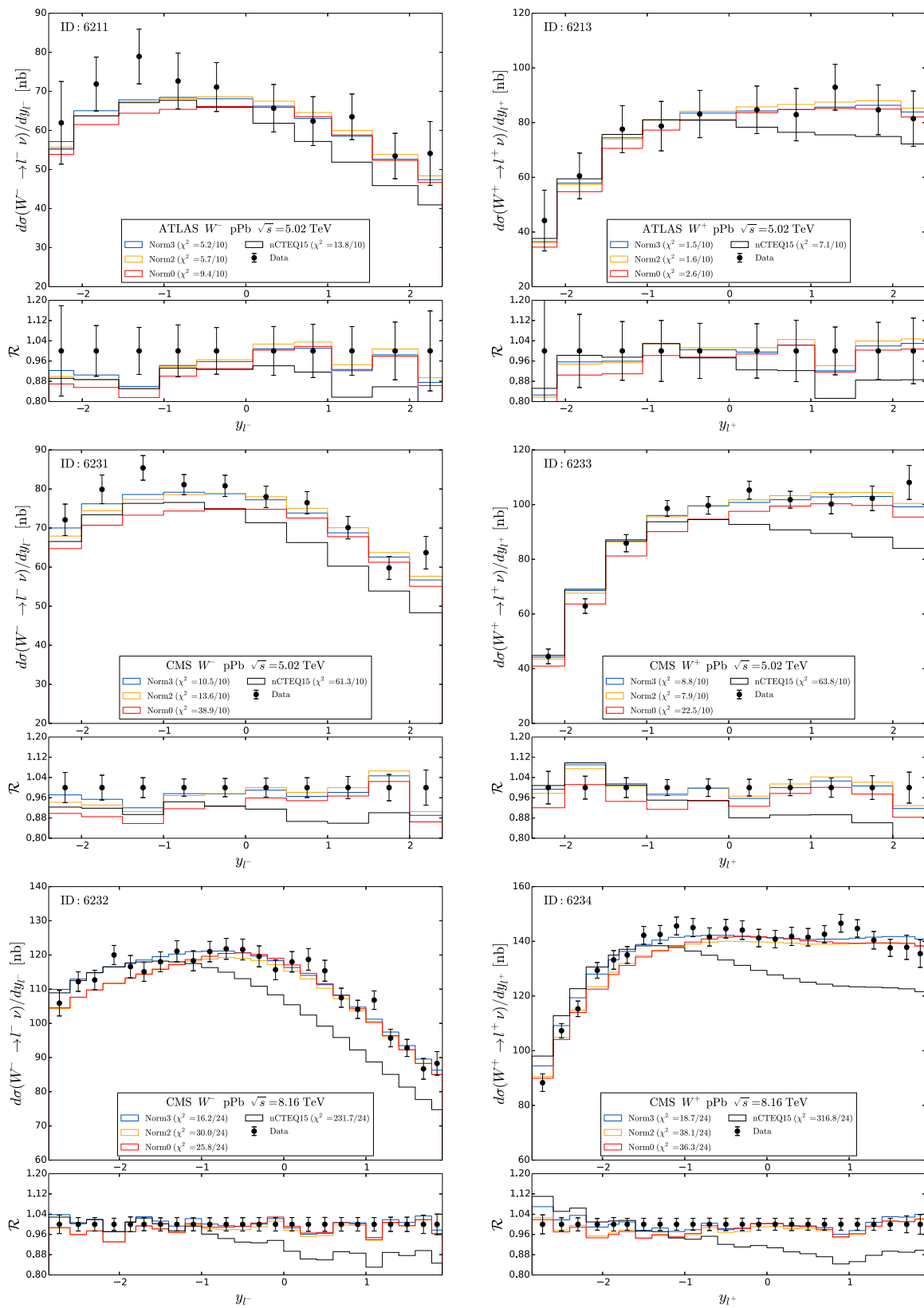


Fig. 3 Comparison of data with theory for ATLAS and CMS W^\pm production. The normalization shifts are applied to the theory so we can compare all the results on a single plot; the data is unal-

tered. For reference, ATLAS Run I $\{W^-, W^+\} = \{6211, 6213\}$, CMS Run I $\{W^-, W^+\} = \{6231, 6233\}$ and CMS Run I $\{W^-, W^+\} = \{6232, 6234\}$

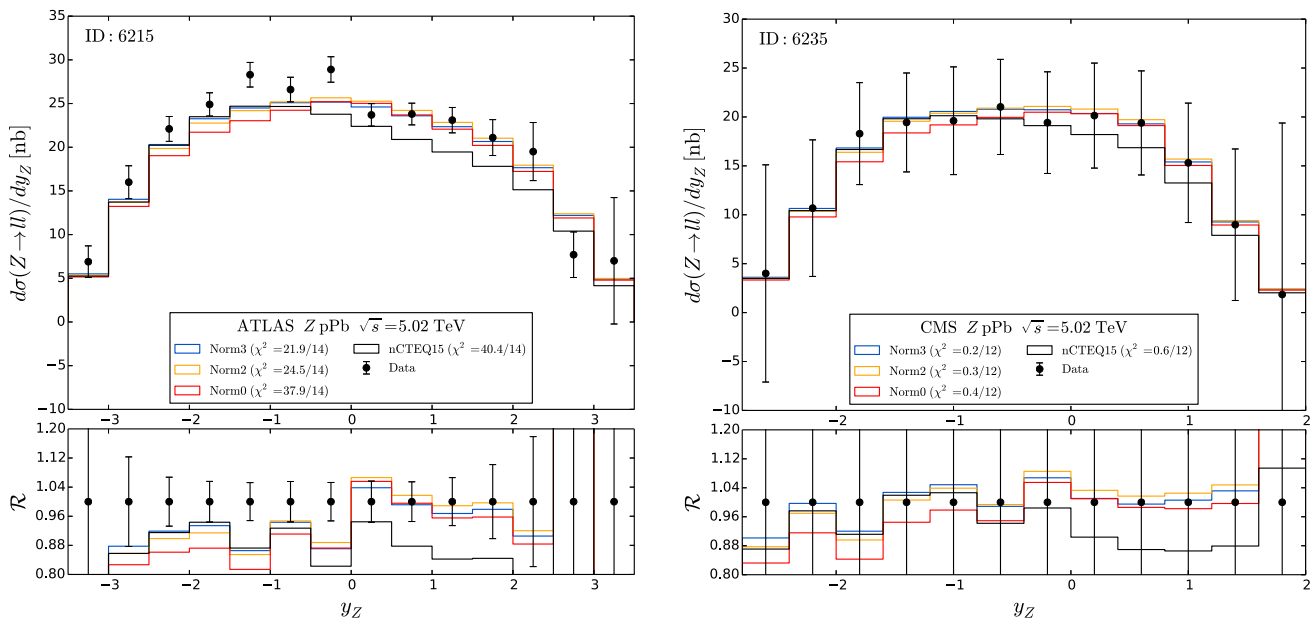


Fig. 4 Comparison of data with theory for ATLAS and CMS Z production. The normalization shifts are applied to the theory so we can compare all the results on a single plot; the data is unaltered. For reference, ATLAS Run I $\{Z\} = \{6215\}$ and CMS Run I $\{Z\} = \{6235\}$

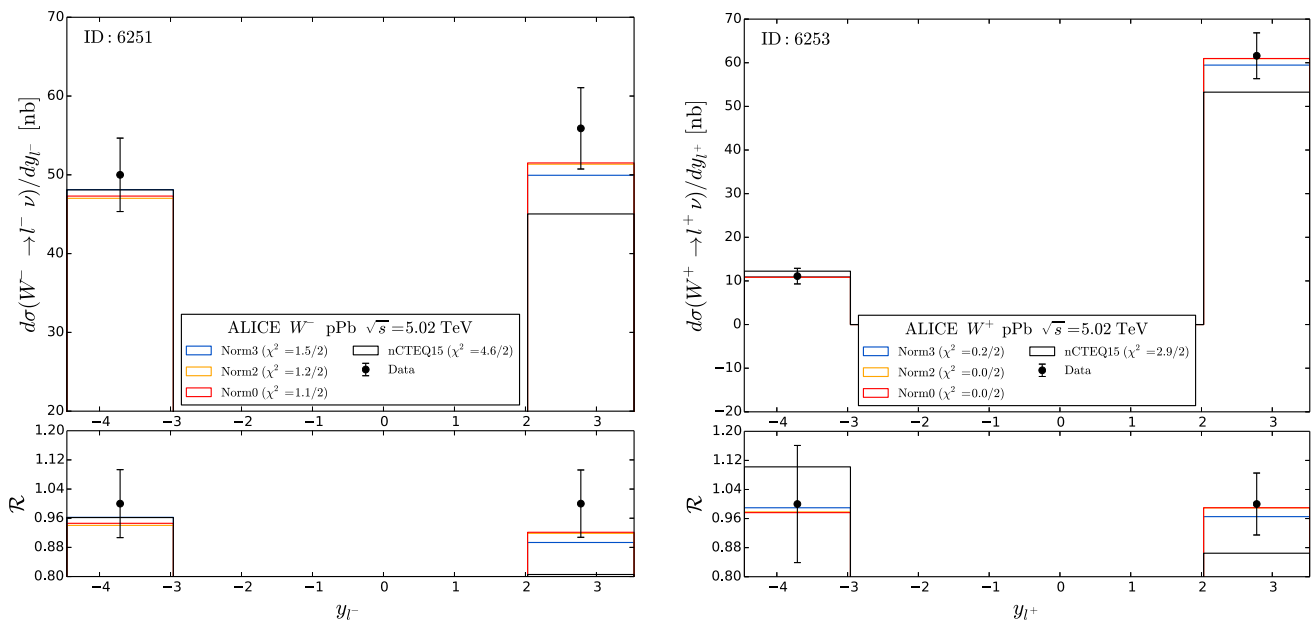


Fig. 5 Comparison of data with theory for ALICE W^\pm production. The normalization shifts are applied to the theory so we can compare all the results on a single plot; the data is unaltered. For reference, ALICE Run I $\{W^-, W^+\} = \{6251, 6253\}$

proton. Thus, not including the nuclear corrections in this region would increase discrepancy.

3.2.2 Small x region

In the large rapidity (small x) region, we generally find good agreement between our new fits and the data. But, this is in striking contrast to the nCTEQ15 PDF which lies well below many of the data points at large y ; this behavior is clearly

evident, for example, in 6215 (ATLAS Z), and 6213, 6232, 6233, 6234 (CMS W^\pm Run I and Run II). Clearly, the new LHC W^\pm/Z data provides important new PDF constraints in this kinematic region that were not available in the nCTEQ15 analysis.

As larger rapidity corresponds to smaller x values, this puts us in the “shadowing region” ($x \lesssim 0.1$) where the nuclear PDFs are generally expected to be suppressed relative to the proton. If the nuclear shadowing correction were

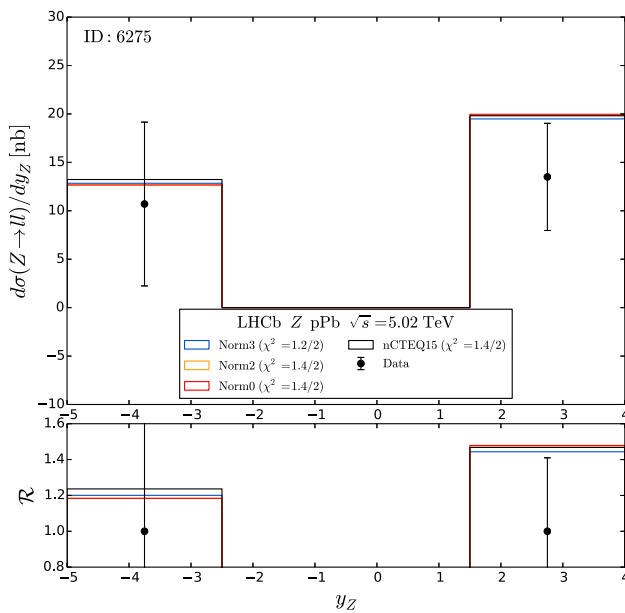


Fig. 6 Comparison of data with theory for LHCb Z production (ID 6275). The normalization shifts are applied to the theory so we can compare all the results on a single plot; the data is unaltered

reduced in this region, that would bring the theory closer in line with the data *without* the need for large normalization factors. The precise value of the nuclear corrections is still an open question; for example, Refs. [42,43,68] found that the shadowing correction for the νN charged-current neutrino DIS was reduced as compared to the $\ell^\pm N$ neutral-current DIS. If such an adjustment were applied to the LHC W^\pm/Z data, it would move the theory closer to the data and reduce the normalization factor. Disentangling the nuclear effects from the underlying parton flavor components is intricate, and a reanalysis of the neutrino DIS data is currently in progress [69].

3.3 The PDFs

Finally, we make a detailed examination of the underlying flavor PDFs from these various fits. In Figs. 7, 8 and 9 we display the nPDFs for a full lead nucleus at three separate scales. The lowest scale ($Q = 2$ GeV) is close to our initial evolution scale of $Q_0 = 1.3$ GeV, the largest scale ($Q = 90$ GeV) is in the range relevant for W^\pm/Z production, and the intermediate scale ($Q = 10$ GeV) helps illustrate the effects of the DGLAP evolution.

We choose to display the full lead nPDF as this is the physical quantity which enters the calculation.⁶ This is computed

⁶ Extracting a “proton in a lead nucleus” may introduce unphysical ambiguities when separating the up and down distributions. In particular, for an isoscalar target, we cannot separately distinguish the u and d distributions.

using:

$$f_i^{(A,Z)}(x, Q) = \frac{Z}{A} f_i^{p/A}(x, Q) + \frac{A-Z}{A} f_i^{n/A}(x, Q), \quad (3)$$

and we assume isospin symmetry to derive the neutron PDF.

3.3.1 Strange and gluon nPDFs

Examining the curves for up and down distributions, we see there is minimal variation between different fits as these flavors are strongly constrained by other data. Interestingly, we also see that the small x uncertainty is reduced at higher scales (see Figs. 8 and 9). We observe a slight modification in the \bar{u} and \bar{d} distributions as these are closely linked to the gluon and strange distributions which we will discuss in the following.

Turning to the gluon and strange PDFs, we see significant differences. In particular, the fits seem to prefer a larger value for both the gluon and strange PDFs at intermediate x values, which is the region relevant for the LHC heavy ion W^\pm/Z production. We discuss these fits in turn.

Norm0: Examining the Norm0 fit for $Q = 2$ GeV (Fig. 7), we see a distinct excess in the strange and gluon PDFs in the region $x \sim 0.03$; this is also evident in Fig. 10 where we have plotted the ratio relative to the nCTEQ15 values. At $Q = 2$ GeV, the peak of the gluon and strange distributions are located at approximately $x \sim 0.03$; via the DGLAP evolution these peaks shift down⁷ to the region $x \sim 0.017$ for $Q = 90$ GeV, consistent with the expectation for the central x value of $\sim M_{W,Z}/\sqrt{s}$.

Recall that the Norm0 fit does not allow any normalization adjustment in the fit. Since the data consistently lie above the theoretical predictions, it appears that the Norm0 fit is exploiting the uncertainty of gluon and strange PDFs to try and pull up the theoretical predictions in line with the data by increasing the PDFs in the relevant x region. Additionally, we observe a similar (but less pronounced) behavior in the \bar{u} and \bar{d} distributions.

As momentum must be conserved, we see the Norm0 strange PDF dips below nCTEQ15 at both high and low x values, while the gluon is below nCTEQ15 at higher x values. Part of the reason the deformation of the gluon and strange PDFs is so large at $Q = 2$ GeV is to compensate for the DGLAP evolution which will tend to diffuse the excess in the gluon and strange distributions at the $Q = 90$ GeV scale, *cf.*, Fig. 9.

Norm2 and Norm3: In contrast to the Norm0 result above, the Norm2 and Norm3 fits allow us to investigate the effect of including the normalization parameters into the fit; this

⁷ For comparison, in the ATLAS proton analysis, the central x value at $\sqrt{s} = 8$ TeV corresponds to $M_{W,Z}/\sqrt{s} \sim 0.023$ at $Q_0 = \sqrt{2}$ GeV, and evolves to $x \sim 0.011$ at $Q \sim M_Z/\sqrt{s}$.

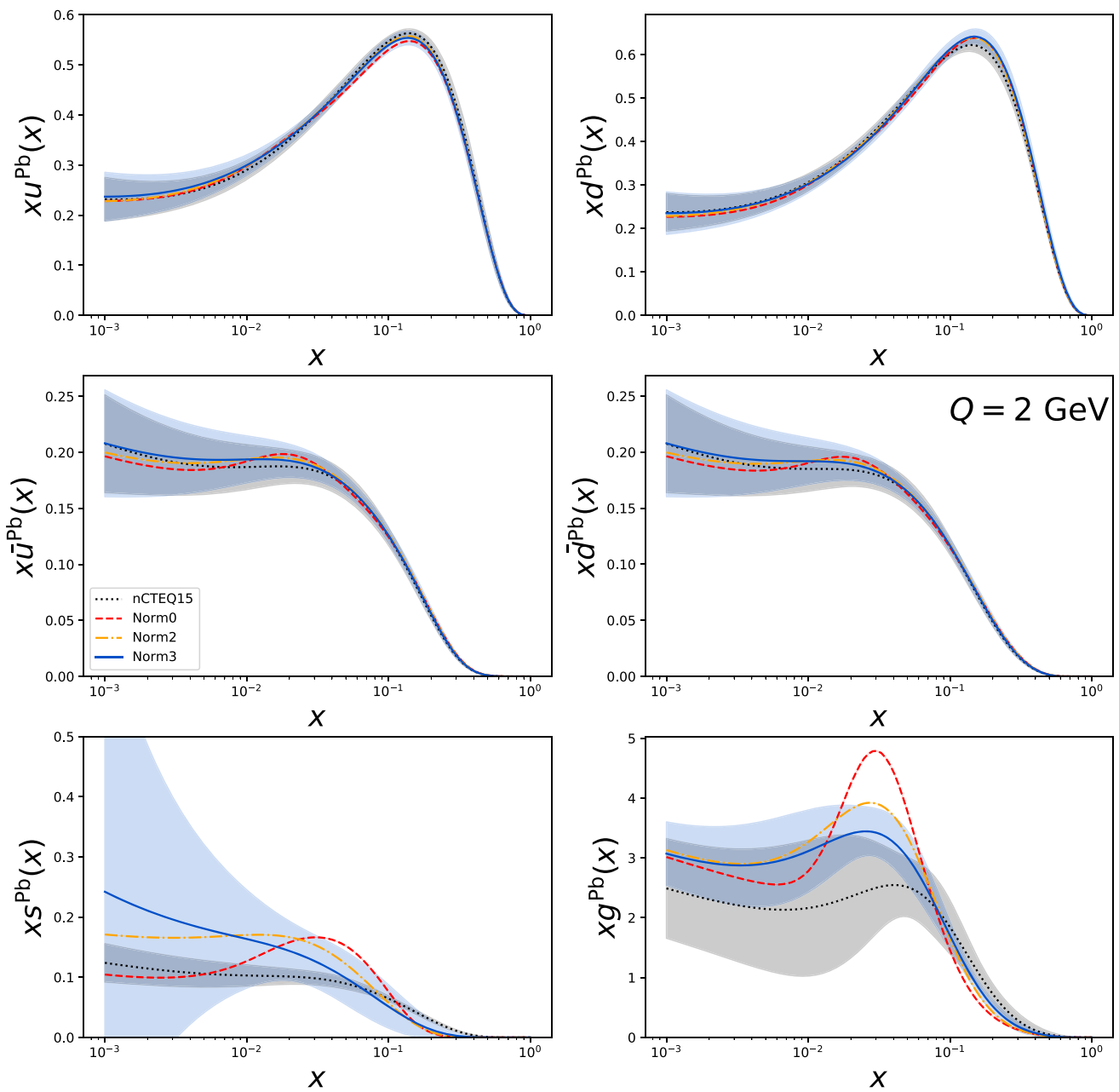


Fig. 7 The full lead (Pb) PDFs for $Q = 2$ GeV. The uncertainty band for nCTEQ15 is shown in gray, and for Norm3 in blue. The increase of the Norm0 set is evident for the strange and gluon PDFs in the region of $x \sim 0.03$

is crucial in reducing the χ^2/N_{dof} for the LHC heavy ion data. The effect on the resulting nPDFs is evident as shown in Fig. 7 where we see that the excess in both the strange and gluon is systematically reduced as we introduce normalization parameters.

In Fig. 7 we also observe the greatly increased error band on the Norm3 strange PDF as compared to nCTEQ15. This counter-intuitive result is due to the additional fitting parameters for the strange quark included in the Norm3 analysis. The nCTEQ15 fit contained minimal data which was sensi-

tive to the strange quark; therefore, it imposed the condition $s \sim \kappa(\bar{u} + \bar{d})/2$ with the boundary condition of $\kappa = 0.5$ for $A = 1$. Consequently, the error bands Fig. 7 reflect only the uncertainty of $(\bar{u} + \bar{d})$, which is comparatively well determined. The phenomena of increasing error bars has been observed in other examples such as the transition from CTEQ6.1 to CTEQ6.6 when additional strange parameters

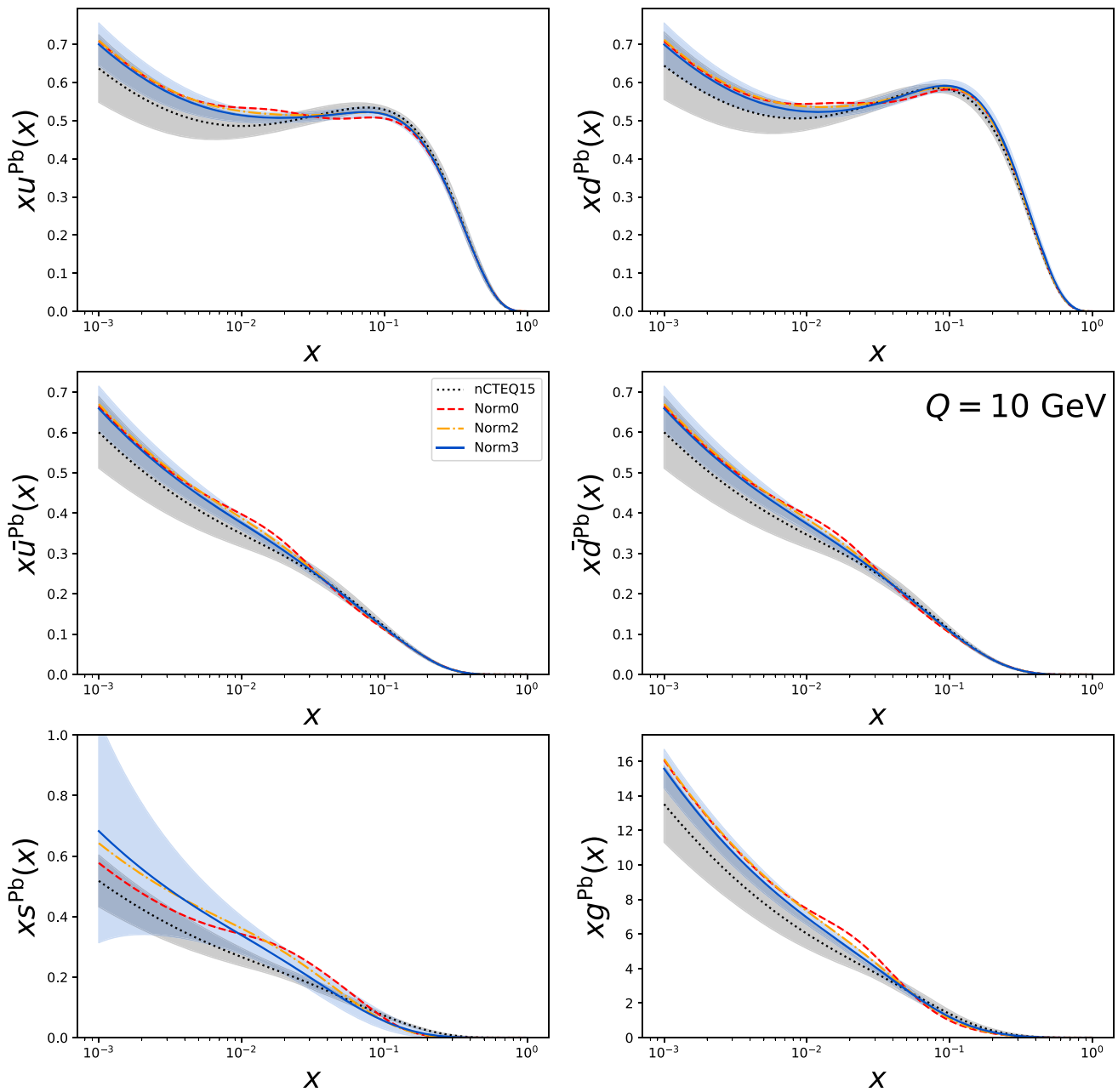


Fig. 8 The full lead (Pb) PDFs for $Q = 10$ GeV. The uncertainty band for nCTEQ15 is shown in gray, and for Norm3 in blue. The increase in the Norm0 set for the strange and gluon PDFs is reduced, compared to the lower Q result, and shifted to smaller $x \sim 0.02$ values

were introduced, or the transition from EPS09 to EPPS16 when additional gluon parameters were introduced.⁸

To highlight the magnitude of these differences, in Fig. 10 we plot the ratios of the PDFs compared to nCTEQ15. At $Q = 2$ GeV, we see that the Norm0 gluon is nearly a factor of 2 times the nCTEQ15 value, with a peak at $x \sim 0.03$.

⁸ See for example, Fig. 1 of Ref. [39] which compares the uncertainty bands of CTEQ6.1 to CTEQ6.6 for the strange PDF, or Fig. 27 of Ref. [6] which compares the uncertainty bands of EPS09 to EPPS16 for the gluon PDF.

The Norm2 and Norm3 gluon PDFs are reduced to $\sim 60\%$ and $\sim 40\%$ above nCTEQ15, respectively.⁹ Similarly, at $x \sim 0.03$ and $Q = 2$ GeV, the strange PDF for both Norm0 and Norm2 are $\sim 60\%$ above the nCTEQ15 value, while the Norm3 result is reduced to $\sim 25\%$.

In Fig. 10 we also display ratio at $Q = 90$ GeV which illustrates the effect of the DGLAP evolution. We see that

⁹ Note we are focusing here on the intermediate x region ($x \gtrsim 0.01$) not only because this is the central x region for W^\pm/Z production, but because the small x region is poorly constrained.

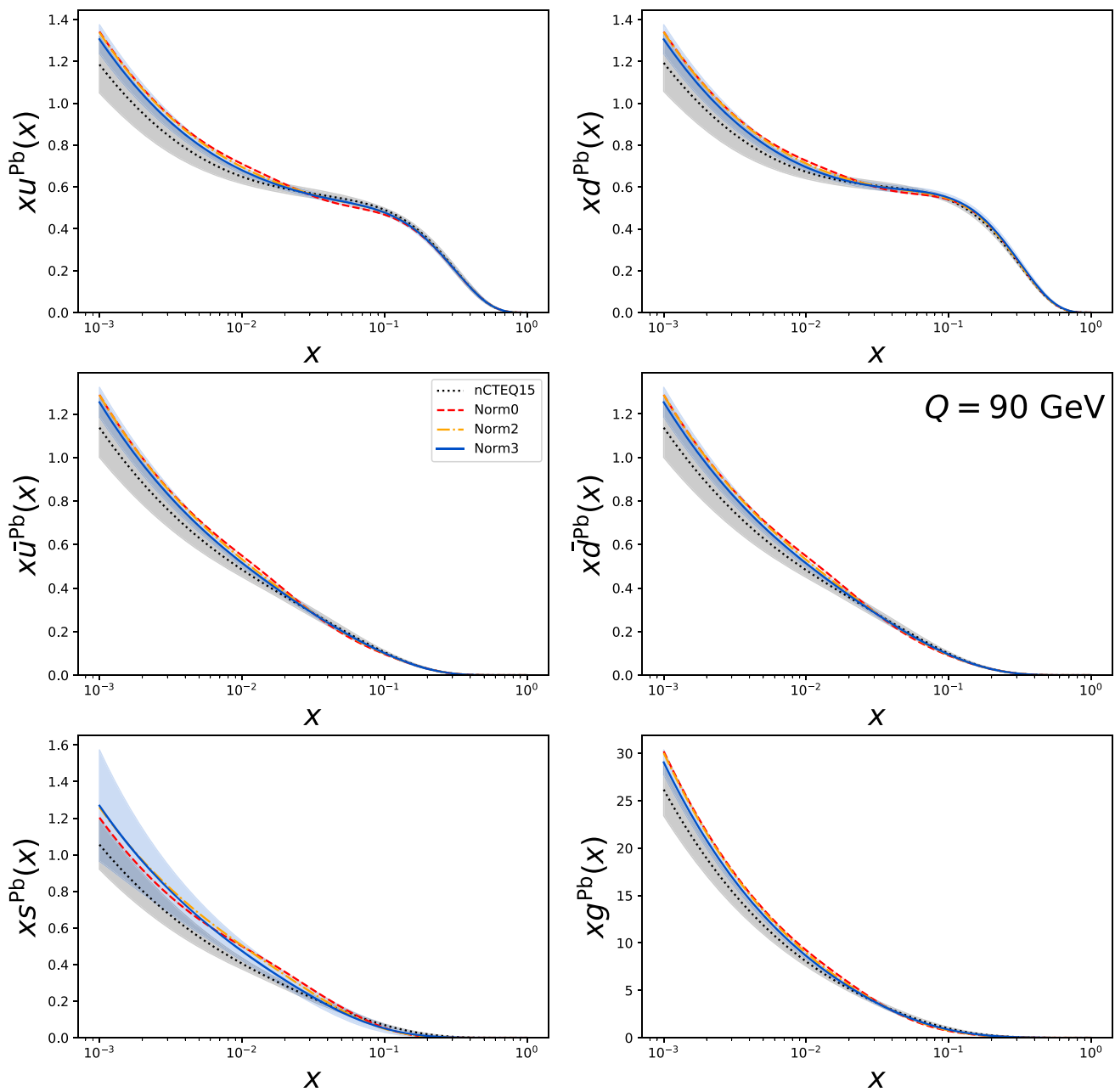


Fig. 9 The full lead (Pb) PDFs for $Q = 90$ GeV. The uncertainty band for nCTEQ15 is shown in gray, and for Norm3 in blue

the gluon is now reduced to $\sim 15\%$ above the nCTEQ15 value, the strange is reduced to $\sim 25\%$ above the nCTEQ15 value, and both peaks have shifted to lower x values.

Because the DGLAP evolution has “washed out” the detailed peak structure at low Q values, it is necessary for the fit to amplify the distortion at low Q so that a remnant of the effect survives at high Q . Nevertheless, the remaining excess at $Q = 90$ GeV is sufficient to improve the χ^2 of the fits.

Additionally, we note that the heavy-flavor reweighting analysis of Ref. [70] also observed an increase of the gluon

nPDF in the intermediate to small x region relative to the nCTEQ15 results. While the shift of the PDF in the reweighting was in the same direction as in this analysis, its magnitude was much smaller.

We now turn our attention to the error band of the gluon distribution in Fig. 10. At NLO, the gluon enters for the first time the W^\pm and Z boson production through the gq initiated contributions. The addition of the W^\pm/Z LHC data to the fit is thus not expected to add significant constraining power for the gluon distribution. Contrary to this naive expectation, due to high center of mass energy and relatively

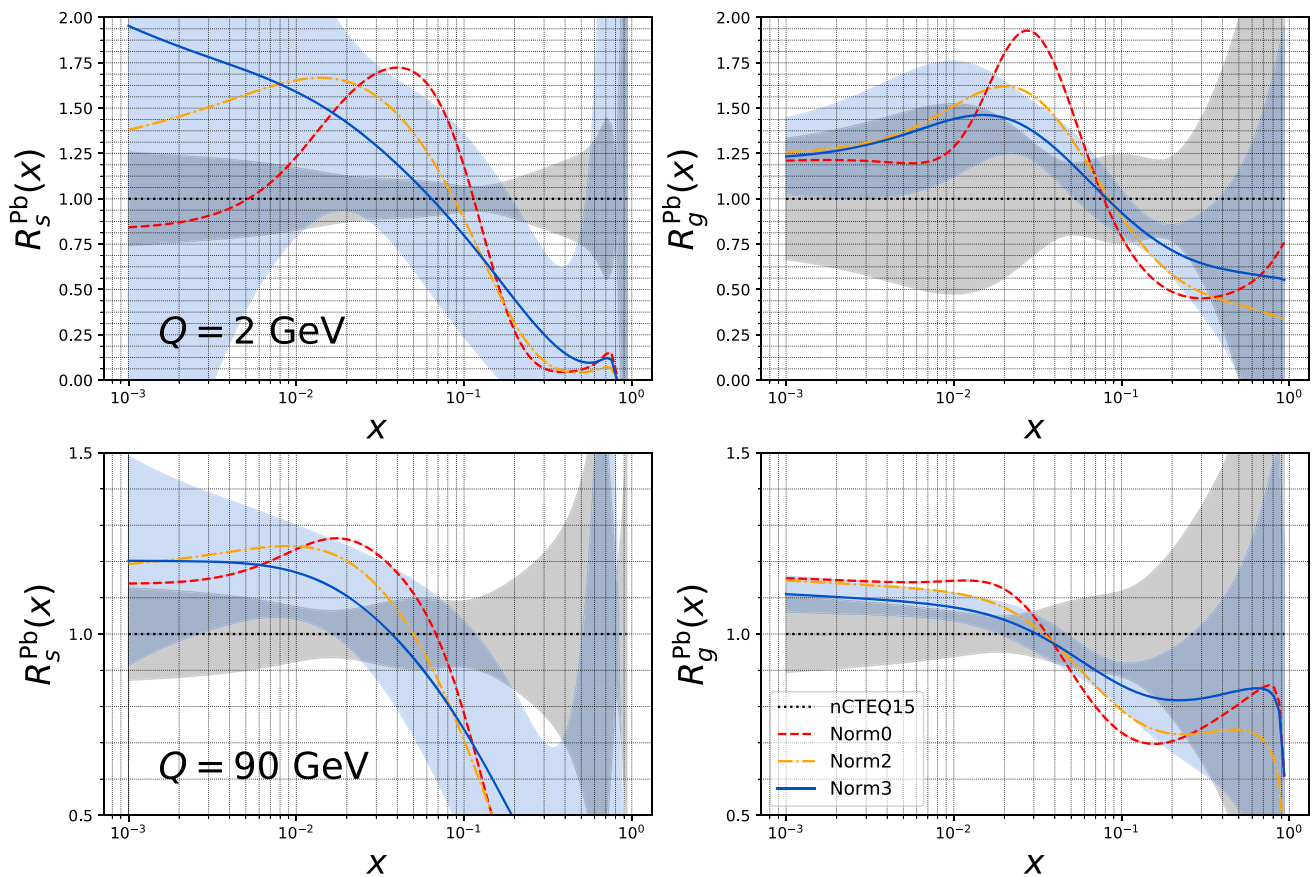


Fig. 10 Ratio of strange and gluon nPDFs compared to the corresponding nCTEQ15 nPDFs for $Q = 2$ GeV (upper row) and $Q = 90$ GeV (lower row). The uncertainty band for nCTEQ15 is shown in gray, and for Norm3 in blue

small values of the probed x , the gluon distribution can have a considerable contribution to W^\pm/Z production processes; this is reflected in the reduced error bands of Norm3 as compared with nCTEQ15. Indeed, an independent variation of the open gluon parameters around the minimum in the Norm3 fit confirms that the χ^2 contribution from the LHC data is similarly steep or steeper than contribution from all the other data included in the fit.¹⁰

4 Comparisons

4.1 Comparison with other nPDFs

Having investigated the impact of the W^\pm/Z heavy ion data including normalization effects, we now compare our PDFs with other results from the literature.

There are a number of nPDF sets available [67,72,73] including some new determinations [7,8,74]. The TUJU19

¹⁰ In fact, this phenomenon is reminiscent of the significant impact of the gluon on the Tevatron high- E_T jet cross sections via the qg -channel as described in Ref. [71].

analysis [74] extends the xFitter framework to include nuclear PDFs; this open-source program provides a valuable tool for the PDF community. As an initial step, TUJU19 assumed $s = \bar{s}$ and $s = \bar{u} = \bar{d}$, and the resulting nPDFs compare favorably with EPPS16 and nCTEQ15 within uncertainties.

A separate effort by the NNPDF collaboration [7,8] uses neural network techniques to extract the gluon and quark nPDFs; this method provides a complementary approach to the traditional parameterized function-based method. Their recent analysis [8] has produced the nNNPDF2.0 nPDF set which includes charged current DIS data from NuTeV (Fe) and Chorus (Pb), and also LHC W^\pm/Z data. They also compute the strangeness ratio, $R_s = (s + \bar{s})/(\bar{u} + \bar{d})$, and find the nuclear value is reduced as compared to the proton. The neutrino DIS data and LHC $W + c$ associated production seem to prefer a lower R_s value, while the inclusive W and Z production favor a larger value. These interesting observations raise some important issues, and additional investigation is warranted to better understand the strange distribution [9].

The EPPS16 data sets include DIS, DY, RHIC inclusive pion, and LHC W^\pm/Z and dijet data; in particular, this set incorporates a number of parameters to provide flexibility

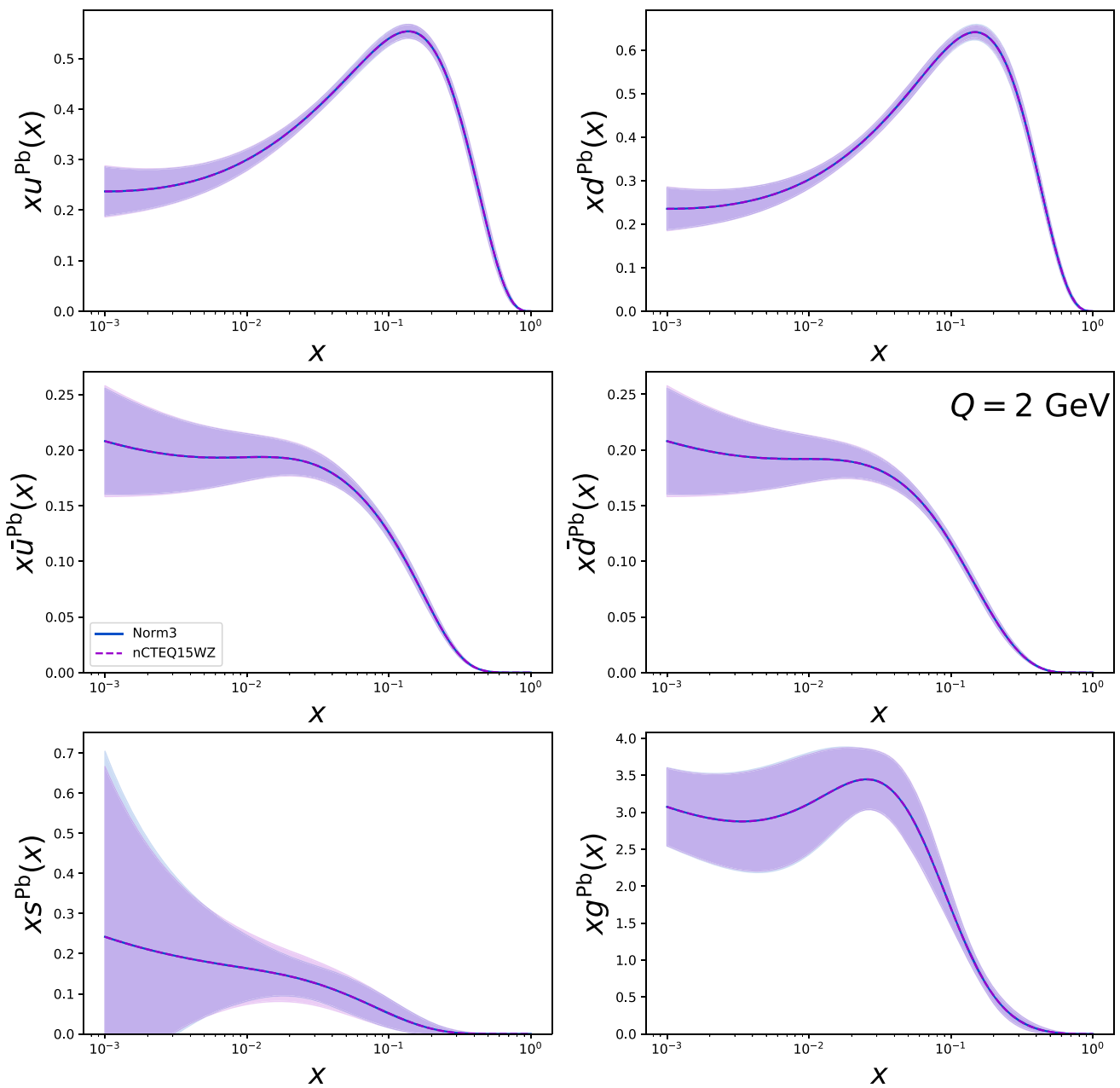


Fig. 11 Comparison of the full lead (Pb) PDFs at $Q = 2$ GeV for nCTEQ15WZ and Norm3 fits. The uncertainty band for nCTEQ15WZ is shown in purple, Norm3 in blue. This shows that the central value of

these fits are essentially identical, and the error bands are also virtually identical with the exception of small differences in the strange quark PDF

in both the strange and gluon PDFs. Therefore, it will be interesting to compare the variation of these flavors between our original nCTEQ15 nPDFs and our nCTEQ15WZ fit.

The nCTEQ15WZ fit is based on the Norm3 fit (with 3 normalization parameters), and in addition includes the RHIC pion data in the fitting loop. The RHIC pion data is fit with the Binnewies–Kniehl–Kramer (BKK) fragmentation functions [75] using a custom gridding technique for fast evaluation

[1]. The resulting nCTEQ15WZ nPDFs are nearly identical as the Norm3 nPDFs which is evident when comparing the χ^2/N_{dof} values of Table 3, as well as the PDFs in Fig. 11.

We now compare the results of our nCTEQ15WZ fit with the nCTEQ15, EPPS16, and nNNPDF2.0 nPDFs in Figs. 12 and 13. To begin, we focus on the plots at $Q = 2$ GeV as the variations are more evident here. For the up and down components $\{u, d, \bar{u}, \bar{d}\}$, nCTEQ15WZ is quite similar to

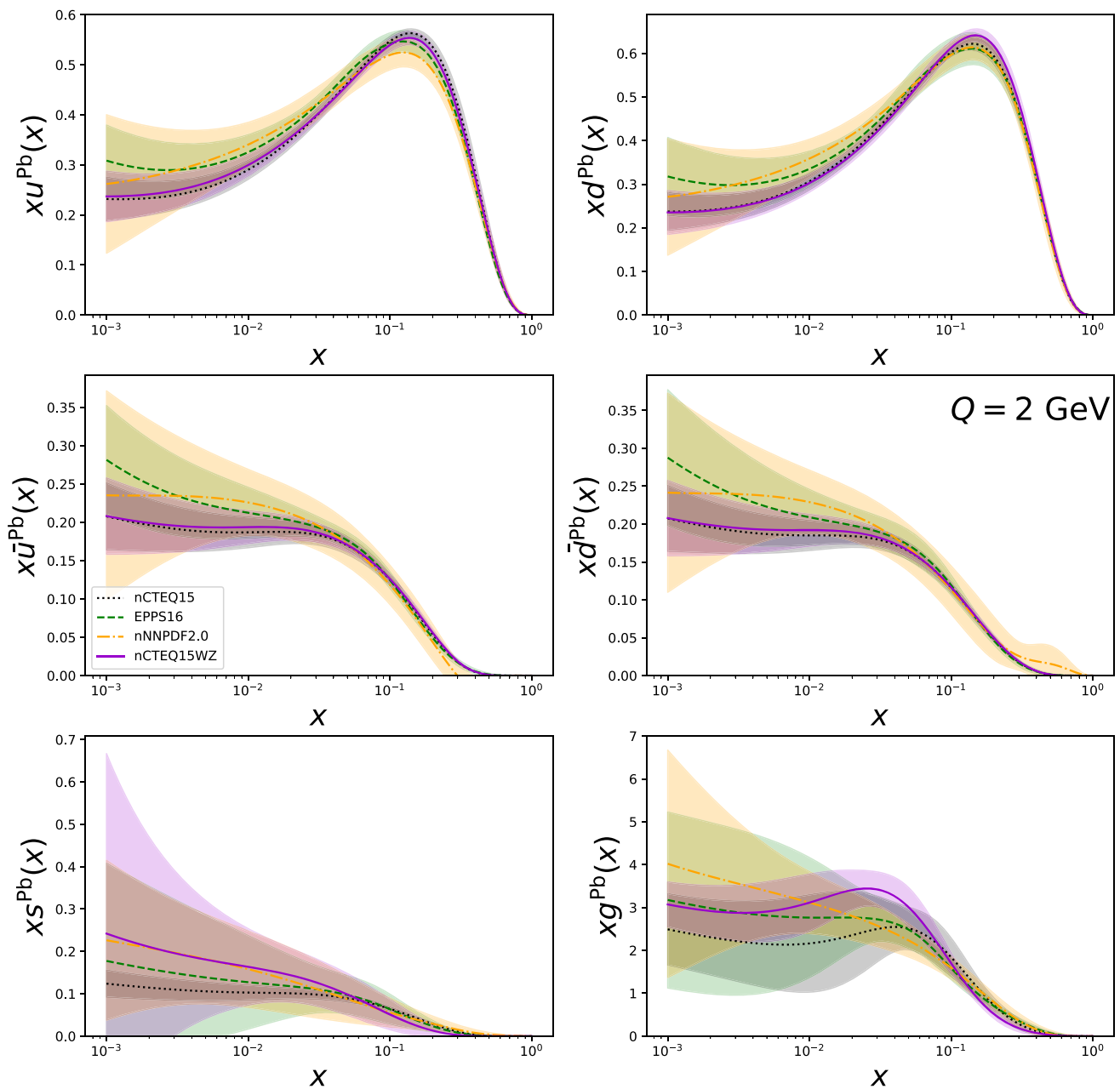


Fig. 12 Comparison of the full lead (Pb) PDFs at $Q = 2$ GeV for nCTEQ15, EPPS16, nNNPDF2.0 and nCTEQ15WZ. The uncertainty band for nCTEQ15 is shown in gray, nCTEQ15WZ in violet, nNNPDF2.0 in yellow and EPPS16 in green

nCTEQ15, and these flavors generally lie below EPPS16 and nNNPDF2.0, but are within uncertainties. As discussed in Sect. 3.3.1, we recall that the nCTEQ15 error bands on the strange PDF are underestimated due to restriction of the parameters. For the strange and gluon, we see that nCTEQ15 and EPPS16 are generally similar for larger x values, and then diverge somewhat for small x . The nCTEQ15WZ nPDFs lie below nCTEQ15 and EPPS16 for large x values, and then above at intermediate to small x values; this allows $s(x)$ and $g(x)$ to increase the W^\pm/Z cross section in the region

of the data ($x \sim 0.02$) while not perturbing the momentum sum rules. nNNPDF2.0 is similar to nCTEQ15 and EPPS16 for large x values, but then increases for smaller x . For the strange distribution, nNNPDF2.0 coincides with nCTEQ15WZ at small x , while for the gluon, nNNPDF2.0 exceeds nCTEQ15WZ at small x . Similar effects to the above are generally evident at larger Q values (Fig. 13), but their magnitude is diminished due to the DGLAP evolution effects.

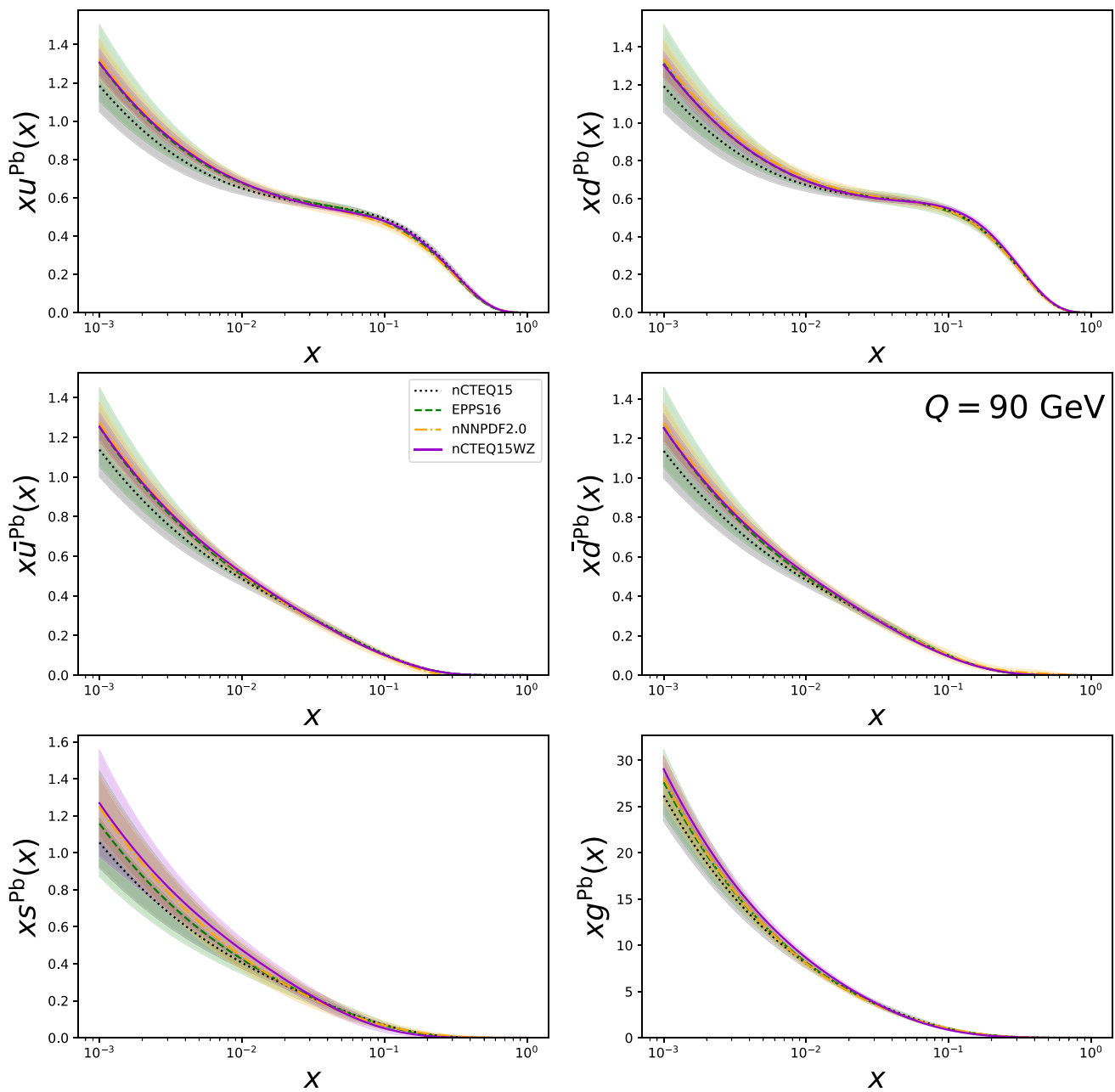


Fig. 13 Comparison of the full lead (Pb) PDFs at $Q = 90$ GeV for nCTEQ15, EPPS16, nNNPDF2.0 and nCTEQ15WZ. The uncertainty band for nCTEQ15 is shown in gray, nCTEQ15WZ in violet, nNNPDF2.0 in yellow and EPPS16 in green

4.2 Comparison with proton results

The strange quark PDF has also been studied extensively for the proton case by many groups including ABM [13], CT18 [4], JAM [15], MMHT [16, 17], and NNPDF [18]. There is a close connection between the proton and nuclear PDFs; for example, nCTEQ15 uses the proton PDF as a boundary condition, and EPPS16 fits nuclear ratios relative to the proton.

One quantity of interest we can compare between the proton and the nuclear PDFs is the ratio of the strange PDF

relative to the light-sea quarks: $R_s = (s + \bar{s})/(\bar{u} + \bar{d})$. A very recent analysis of the proton strange PDF was presented in Ref. [76] which includes the LHC inclusive W^\pm/Z production and associated $W + c$ channel, as well as neutrino DIS data from NuTeV and NOMAD; this study obtains $R_s = 0.78 \pm 0.20$. In Fig. 14, we compute R_s for selected Q values, and compare this to the proton result as extracted by ATLAS [31, 77].

Comparing the proton and the lead results at $Q^2 = 1.9 \text{ GeV}^2$, we see that the behavior of the Norm3 curve

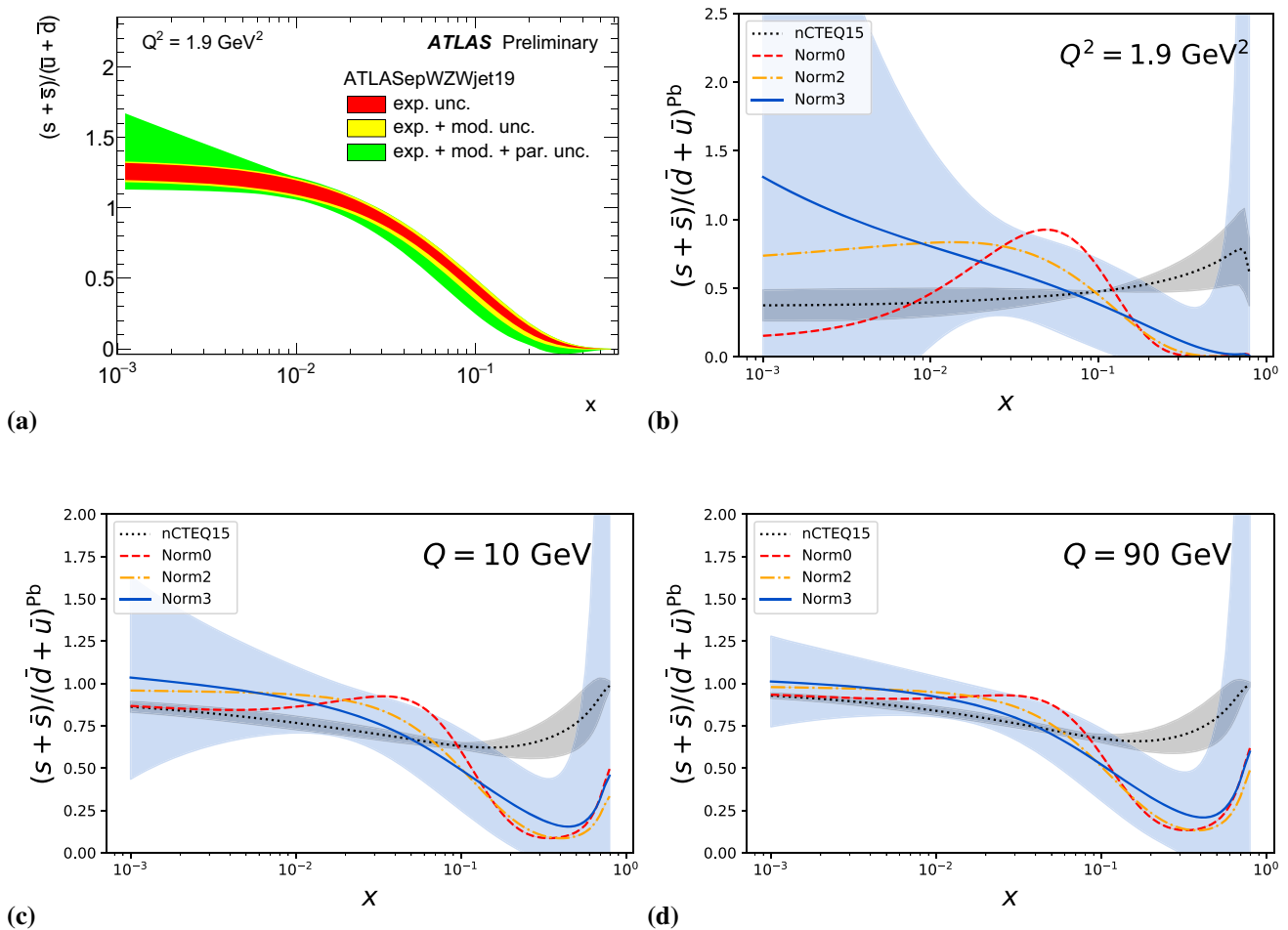


Fig. 14 **a** Recent (preliminary) result from ATLAS on the strange ratio for the proton [31]. **b** The nuclear strange ratio for lead (Pb) nPDFs as obtained in our fits. The uncertainty band for nCTEQ15 is shown in gray, and Norm3 in blue

(panel-b) is quite similar to the proton result (panel-a). In contrast, the nCTEQ15 result is generally flat across all x values as the strange was set to be a fixed fraction of the u/d -sea PDFs, $s = \bar{s} = \kappa(\bar{u} + \bar{d})/2$. Additionally, we also display the other fits, Norm0 and Norm2, to illustrate the range of possible variations. The uncertainty bands for Norm3 are displayed; these are large for small x , where the strange is poorly constrained, and also at very large x where the quark sea denominator vanishes. We also display larger Q values which illustrates the convergent effects of the DGLAP evolution.

In the previous section we raised the question as to whether the enhanced strange distribution was reflecting the true underlying physics, or was instead an artifact of the fit. The similarities of R_s between the proton and lead PDFs may indicate that the enhanced strange PDF is, in fact, a real effect. To definitively answer this question will require additional analysis, and this work is ongoing.

5 Conclusion

Our ability to fully characterize fundamental observables, like the Higgs boson couplings and the W boson mass, and to constrain both SM and BSM signatures is strongly limited by how accurately we determine the underlying PDFs [78]. A precise determination of the strange PDF is an important step in advancing these measurements.

The new nCTEQ++ framework allowed us to include the LHC W/Z data directly in the fit. While these new fits significantly reduced the overall χ^2 for the W/Z LHC data, we still observe tensions in individual data sets which require further investigation. Our analysis has identified factors which might further reduce the apparent discrepancies including: increasing the strange PDF, modifying the nuclear correction, and adjusting the data normalization.

Compared to the nCTEQ15 PDFs, these new fits favor an increased strange and gluon distribution in the x region relevant for heavy ion W^\pm/Z production. While we obtain a good fit in terms of the overall χ^2 values, we must ask: i) how

the uncertainties and data normalization affect the resulting PDFs, and ii) whether the results truly reflect the underlying physics, or is the fit simply exploiting $s(x)$ because that is one of the least constrained flavors? The answer to this important question will require additional study; this is currently under investigation.

The LHAPDF files of the resulting nCTEQ15WZ nPDFs will be made available at the nCTEQ website www.ncteq.org which is hosted at HepForge.org.

Acknowledgements We are pleased to thank Aaron Angerami, Émilien Chapon, Cynthia Keppel, Jorge Morfin, Pavel Nadolsky, Jeff Owens and Mark Sutton for help and useful discussion. A.K. is grateful for the support of the Kosciuszko Foundation. A.K. also acknowledges partial support by Narodowe Centrum Nauki grant UMO-2019/34/E/ST2/00186. The work of T.J. was supported by the Deutsche Forschungsgemeinschaft (DFG, German Research Foundation) under grant 396021762-TRR 257. Work at WWU Münster was funded by the Deutsche Forschungsgemeinschaft (DFG, German Research Foundation) through Project-Id 273811115-SFB 1225 and the Research Training Network 2149 “Strong and weak interactions-from hadrons to dark matter”. T.J.H. and F.O. acknowledge support through US DOE grant DE-SC0010129. T.J.H. also acknowledges support from a JLab EIC Center Fellowship.

Data Availability Statement This manuscript has no associated data or the data will not be deposited. [Authors’ comment: The nPDFs will be posted at lhappdf.hepforge.org and on ncteq.org. The data used in this fit are posted at hepdata.net. Therefore, all the data associated with this publication will be stored in long-term repositories.]

Open Access This article is licensed under a Creative Commons Attribution 4.0 International License, which permits use, sharing, adaptation, distribution and reproduction in any medium or format, as long as you give appropriate credit to the original author(s) and the source, provide a link to the Creative Commons licence, and indicate if changes were made. The images or other third party material in this article are included in the article’s Creative Commons licence, unless indicated otherwise in a credit line to the material. If material is not included in the article’s Creative Commons licence and your intended use is not permitted by statutory regulation or exceeds the permitted use, you will need to obtain permission directly from the copyright holder. To view a copy of this licence, visit <http://creativecommons.org/licenses/by/4.0/>. Funded by SCOAP³.

A Fitting data normalizations

When fitting the normalization of data sets, we use the χ^2 prescription given in Ref. [79]. For a data set D with N data points and S correlated systematic errors, the χ^2 of the data set reads:

$$\chi_D^2 = \sum_{i,j}^N \left(D_i - \frac{T_i}{N_{norm}} \right) (C^{-1})_{ij} \left(D_j - \frac{T_j}{N_{norm}} \right) + \left(\frac{1 - N_{norm}}{\sigma_{norm}} \right)^2 \tag{4}$$

where σ_{norm} is the normalization uncertainty and T_i is the theoretical prediction for point i . We take the normalization uncertainty σ_{norm} to be the experimental luminosity uncertainty as listed in Table 2. The last term of Eq. (4) is called the normalization penalty and it enters when the fitted normalization, N_{norm} , differs from unity. The normalization uncertainty σ_{norm} appearing in the denominator prevents large excursions of N_{norm} away from unity.

The covariance matrix C_{ij} is defined as:

$$C_{ij} = \sigma_i^2 \delta_{ij} + \sum_{\alpha}^S \bar{\sigma}_{i\alpha} \bar{\sigma}_{j\alpha} \tag{5}$$

where σ_i is the total uncorrelated uncertainty (added in quadrature) for data point i , and $\bar{\sigma}_{i\alpha}$ is the correlated systematic uncertainty for data point i from source α . Using the analytical formula for the inverse of the correlation matrix as in Ref. [80], we obtain:

$$\chi_D^2 = \sum_i \left(\frac{D_i - T_i/N_{norm}}{\sigma_i} \right)^2 - B^T A^{-1} B + \left(\frac{1 - N_{norm}}{\sigma_{norm}} \right)^2, \tag{6}$$

with

$$A_{\alpha\gamma} = \delta_{\alpha\gamma} + \sum_i \frac{\bar{\sigma}_{i\alpha} \bar{\sigma}_{i\gamma}}{\sigma_i^2}, \tag{7}$$

and

$$B_{\alpha} = \sum_i \frac{\bar{\sigma}_{i\alpha} (D_i - T_i/N_{norm})}{\sigma_i^2}. \tag{8}$$

References

1. K. Kovarik et al., nCTEQ15: Global analysis of nuclear parton distributions with uncertainties in the CTEQ framework. Phys. Rev. D **93**(8), 085037 (2016). [arXiv:1509.00792](https://arxiv.org/abs/1509.00792) [hep-ph]
2. R. Gavin, Y. Li, F. Petriello, S. Quackenbush, W Physics at the LHC with FEWZ 2.1. Comput. Phys. Commun. **184**, 208–214 (2013). [arXiv:1201.5896](https://arxiv.org/abs/1201.5896) [hep-ph]
3. R. Gavin, Y. Li, F. Petriello, S. Quackenbush, FEWZ 2.0: A code for hadronic Z production at next-to-next-to-leading order. Comput. Phys. Commun. **182**, 2388–2403 (2011). [arXiv:1011.3540](https://arxiv.org/abs/1011.3540) [hep-ph]
4. T.-J. Hou et al., New CTEQ global analysis of quantum chromodynamics with high-precision data from the LHC. [arXiv:1912.10053](https://arxiv.org/abs/1912.10053) [hep-ph]
5. NNPDF Collaboration, R.D. Ball et al., Parton distributions from high-precision collider data. Eur. Phys. J. C **77**(10), 663 (2017). [arXiv:1706.00428](https://arxiv.org/abs/1706.00428) [hep-ph]
6. K.J. Eskola, P. Paakkinen, H. Paukkunen, C.A. Salgado, EPPS16: Nuclear parton distributions with LHC data. Eur. Phys. J. C **77**(3), 163 (2017). [arXiv:1612.05741](https://arxiv.org/abs/1612.05741) [hep-ph]
7. NNPDF Collaboration, R. Abdul Khalek, J.J. Ethier, J. Rojo, Nuclear parton distributions from lepton-nucleus scattering and the impact of an electron-ion collider. Eur. Phys. J. C **79**(6), 471 (2019). [arXiv:1904.00018](https://arxiv.org/abs/1904.00018) [hep-ph]

8. R. Abdul Khalek, J.J. Ethier, J. Rojo, G. van Weelden, nNNPDF2.0: Quark Flavor Separation in Nuclei from LHC Data. [arXiv:2006.14629](#) [hep-ph]
9. J.J. Ethier, E.R. Nocera, Parton Distributions in Nucleons and Nuclei. *Ann. Rev. Nucl. Part. Sci.* **70**, 1–34 (2020). [arXiv:2001.07722](#) [hep-ph]
10. R. Abdul Khalek, S. Bailey, J. Gao, L. Harland-Lang, J. Rojo, Towards ultimate parton distributions at the high-luminosity LHC. *Eur. Phys. J. C* **78**(11), 962 (2018). [arXiv:1810.03639](#) [hep-ph]
11. J. Gao, L. Harland-Lang, J. Rojo, The structure of the proton in the LHC precision era. *Phys. Rept.* **742**, 1–121 (2018). [arXiv:1709.04922](#) [hep-ph]
12. K. Kovarik, P.M. Nadolsky, D.E. Soper, Hadron structure in high-energy collisions. [arXiv:1905.06957](#) [hep-ph]
13. S. Alekhin, J. Blümlein, S. Moch, Strange sea determination from collider data. *Phys. Lett. B* **777**, 134–140 (2018). [arXiv:1708.01067](#) [hep-ph]
14. P.M. Nadolsky, H.-L. Lai, Q.-H. Cao, J. Huston, J. Pumplin, D. Stump, W.-K. Tung, C.-P. Yuan, Implications of CTEQ global analysis for collider observables. *Phys. Rev. D* **78**, 013004 (2008). [arXiv:0802.0007](#) [hep-ph]
15. JAM Collaboration, N. Sato, C. Andres, J. Ethier, W. Melnitchouk, Strange quark suppression from a simultaneous Monte Carlo analysis of parton distributions and fragmentation functions. *Phys. Rev. D* **101**(7), 074020 (2020). [arXiv:1905.03788](#) [hep-ph]
16. L. Harland-Lang, A. Martin, P. Motylinski, R. Thorne, Parton distributions in the LHC era: MMHT 2014 PDFs. *Eur. Phys. J. C* **75**(5), 204 (2015). [arXiv:1412.3989](#) [hep-ph]
17. R.S. Thorne, S. Bailey, T. Cridge, L.A. Harland-Lang, A. Martin, R. Nathvani, Updates of PDFs using the MMHT framework. *PoS DIS2019 036* (2019). [arXiv:1907.08147](#) [hep-ph]
18. NNPDF Collaboration, R.D. Ball, L. Del Debbio, S. Forte, A. Guffanti, J.I. Latorre, A. Piccione, J. Rojo, M. Ubiali, Precision determination of electroweak parameters and the strange content of the proton from neutrino deep-inelastic scattering. *Nucl. Phys. B* **823**, 195–233 (2009). [arXiv:0906.1958](#) [hep-ph]
19. H.-W. Lin et al., Parton distributions and lattice QCD calculations: a community white paper. *Prog. Part. Nucl. Phys.* **100**, 107–160 (2018). [arXiv:1711.07916](#) [hep-ph]
20. H.-W. Lin et al., Parton distributions and lattice QCD calculations: toward 3D structure. [arXiv:2006.08636](#) [hep-ph]
21. J. Rafelski, B. Muller, Strangeness Production in the Quark - Gluon Plasma. *Phys. Rev. Lett.* **48**, 1066 (1982). [Erratum: *Phys. Rev. Lett.* **56**, 2334 (1986)]
22. M. Deák, K. Kutak, K. Tywoniuk, Towards tomography of quark-gluon plasma using double inclusive forward-central jets in Pb-Pb collision. *Eur. Phys. J. C* **77**(11), 793 (2017). [arXiv:1706.08434](#) [hep-ph]
23. C. Gale, J.-F. Paquet, B. Schenke, C. Shen, Probing Early-Time Dynamics and Quark-Gluon Plasma Transport Properties with Photons and Hadrons, in 28th International Conference on Ultrarelativistic Nucleus-Nucleus Collisions. 2, (2020). [arXiv:2002.05191](#) [hep-ph]
24. A. Bhattacharya, R. Enberg, Y.S. Jeong, C. Kim, M.H. Reno, I. Sarcevic, A. Stasto, Prompt atmospheric neutrino fluxes: perturbative QCD models and nuclear effects. *JHEP* **11**, 167 (2016). [arXiv:1607.00193](#) [hep-ph]
25. V. Bertone, R. Gauld, J. Rojo, Neutrino Telescopes as QCD Microscopes. *JHEP* **01**, 217 (2019). [arXiv:1808.02034](#) [hep-ph]
26. M.H. Reno, J.F. Krizmanic, T.M. Venters, Cosmic tau neutrino detection via Cherenkov signals from air showers from Earth-emerging taus. *Phys. Rev. D* **100**(6), 063010 (2019). [arXiv:1902.11287](#) [astro-ph.HE]
27. W. Bai, M. Diwan, M.V. Garzelli, Y.S. Jeong, M.H. Reno, Far-forward neutrinos at the Large Hadron Collider. *JHEP* **06**, 032 (2020). [arXiv:2002.03012](#) [hep-ph]
28. PROSA Collaboration, O. Zenaiev, M. Garzelli, K. Lipka, S. Moch, A. Cooper-Sarkar, F. Olness, A. Geiser, G. Sigl, Improved constraints on parton distributions using LHCb, ALICE and HERA heavy-flavour measurements and implications for the predictions for prompt atmospheric-neutrino fluxes. *JHEP* **04**, 118 (2020). [arXiv:1911.13164](#) [hep-ph]
29. ATLAS Collaboration, G. Aad et al., Determination of the strange quark density of the proton from ATLAS measurements of the $W \rightarrow \ell\nu$ and $Z \rightarrow \ell\ell$ cross sections. *Phys. Rev. Lett.* **109**, 012001 (2012). [arXiv:1203.4051](#) [hep-ex]
30. ATLAS Collaboration, M. Aaboud et al., Precision measurement and interpretation of inclusive W^+ , W^- and Z/γ^* production cross sections with the ATLAS detector. *Eur. Phys. J. C* **77**(6), 367 (2017). [arXiv:1612.03016](#) [hep-ex]
31. ATLAS Collaboration, T. A. collaboration, QCD analysis of ATLAS W^\pm boson production data in association with jets
32. NuTeV Collaboration, M. Tzanov et al., Precise measurement of neutrino and anti-neutrino differential cross sections. *Phys. Rev. D* **74**, 012008 (2006). [arXiv:hep-ex/0509010](#) [hep-ex]
33. NuTeV Collaboration, D. Mason et al., Measurement of the nucleon strange-antistrange asymmetry at next-to-leading order in QCD from NuTeV dimuon data. *Phys. Rev. Lett.* **99**, 192001 (2007)
34. NuTeV Collaboration, M. Goncharov et al., Precise Measurement of Dimuon Production Cross-Sections in ν_μ Fe and $\bar{\nu}_\mu$ Fe Deep Inelastic Scattering at the Tevatron. *Phys. Rev. D* **64**, 112006 (2001). [arXiv:hep-ex/0102049](#) [hep-ex]
35. HERMES Collaboration, A. Airapetian et al., Measurement of Parton Distributions of Strange Quarks in the Nucleon from Charged-Kaon Production in Deep-Inelastic Scattering on the Deuteron. *Phys. Lett. B* **666**, 446–450 (2008). [arXiv:0803.2993](#) [hep-ex]
36. ATLAS Collaboration, G. Aad et al., Measurement of the production of a W boson in association with a charm quark in pp collisions at $\sqrt{s} = 7$ TeV with the ATLAS detector. *JHEP* **05**, 068 (2014). [arXiv:1402.6263](#) [hep-ex]
37. CMS Collaboration, S. Chatrchyan et al., Measurement of Associated $W +$ Charm Production in pp Collisions at $\sqrt{s} = 7$ TeV. *JHEP* **02**, 013 (2014). [arXiv:1310.1138](#) [hep-ex]
38. CMS Collaboration, A.M. Sirunyan et al., Measurement of associated production of a W boson and a charm quark in proton-proton collisions at $\sqrt{s} = 13$ TeV. *Eur. Phys. J. C* **79**(3), 269 (2019). [arXiv:1811.10021](#) [hep-ex]
39. A. Kusina, T. Stavreva, S. Berge, F.I. Olness, I. Schienbein, K. Kovarik, T. Jezo, J.Y. Yu, K. Park, Strange Quark PDFs and Implications for Drell-Yan Boson Production at the LHC. *Phys. Rev. D* **85**, 094028 (2012). [arXiv:1203.1290](#) [hep-ph]
40. A.M. Cooper-Sarkar, K. Wichmann, QCD analysis of the ATLAS and CMS W^\pm and Z cross-section measurements and implications for the strange sea density. *Phys. Rev. D* **98**(1), 014027 (2018). [arXiv:1803.00968](#) [hep-ex]
41. S. Alekhin et al., HERAFitter. *Eur. Phys. J. C* **75**(7), 304 (2015). [arXiv:1410.4412](#) [hep-ph]
42. K. Kovarik, I. Schienbein, F.I. Olness, J.Y. Yu, C. Keppel, J.G. Morfin, J.F. Owens, T. Stavreva, Nuclear corrections in neutrino-nucleus DIS and their compatibility with global NPDF analyses. *Phys. Rev. Lett.* **106**, 122301 (2011). [arXiv:1012.0286](#) [hep-ph]
43. I. Schienbein, J.Y. Yu, K. Kovarik, C. Keppel, J.G. Morfin, F. Olness, J.F. Owens, PDF nuclear corrections for charged and neutral current processes. *Phys. Rev. D* **80**, 094004 (2009). [arXiv:0907.2357](#) [hep-ph]
44. N. Kalantarians, C. Keppel, M.E. Christy, Comparison of the Structure Function F2 as Measured by Charged Lepton and Neutrino Scattering from Iron Targets. *Phys. Rev. C* **96**(3), 032201 (2017). [arXiv:1706.02002](#) [hep-ph]
45. H. Paukkunen, C.A. Salgado, Agreement of Neutrino Deep Inelastic Scattering Data with Global Fits of Parton Distributions. *Phys. Rev. Lett.* **110**(21), 212301 (2013). [arXiv:1302.2001](#) [hep-ph]

46. H. Paukkunen, C.A. Salgado, Compatibility of neutrino DIS data and global analyses of parton distribution functions. *JHEP* **07**, 032 (2010). [arXiv:1004.3140](#) [hep-ph]
47. A. Kusina, F. Lyonnet, D.B. Clark, E. Godat, T. Jezo, K. Kovarik, F.I. Olness, I. Schienbein, J.Y. Yu, Vector boson production in pPb and PbPb collisions at the LHC and its impact on nCTEQ15 PDFs. *Eur. Phys. J. C* **77**(7), 488 (2017). [arXiv:1610.02925](#) [nucl-th]
48. F. Olness, J. Pumplin, D. Stump, J. Huston, P.M. Nadolsky, H.L. Lai, S. Kretzer, J.F. Owens, W.K. Tung, Neutrino dimuon production and the strangeness asymmetry of the nucleon. *Eur. Phys. J. C* **40**, 145–156 (2005). [arXiv:hep-ph/0312323](#) [hep-ph]
49. G.P. Salam, J. Rojo, A Higher Order Perturbative Parton Evolution Toolkit (HOPPET). *Comput. Phys. Commun.* **180**, 120–156 (2009). [arXiv:0804.3755](#) [hep-ph]
50. T. Carli, D. Clements, A. Cooper-Sarkar, C. Gwenlan, G.P. Salam, F. Siegert, P. Starovoitov, M. Sutton, A posteriori inclusion of parton density functions in NLO QCD final-state calculations at hadron colliders: The APPLGRID Project. *Eur. Phys. J. C* **66**, 503–524 (2010). [arXiv:0911.2985](#) [hep-ph]
51. J.M. Campbell, R.K. Ellis, W.T. Giele, A multi-threaded version of MCFM. *Eur. Phys. J. C* **75**(6), 246 (2015). [arXiv:1503.06182](#) [physics.comp-ph]
52. ATLAS Collaboration, Measurement of $W \rightarrow \mu\nu$ production in p+Pb collision at $\sqrt{s_{NN}} = 5.02$ TeV with ATLAS detector at the LHC. ATLAS-CONF-2015-056
53. ATLAS Collaboration, G. Aad et al., Z boson production in p+Pb collisions at $\sqrt{s_{NN}} = 5.02$ TeV measured with the ATLAS detector. *Phys. Rev. C* **92**(4), 044915 (2015). [arXiv:1507.06232](#) [hep-ex]
54. CMS Collaboration, V. Khachatryan et al., Study of W boson production in pPb collisions at $\sqrt{s_{NN}} = 5.02$ TeV. *Phys. Lett. B* **750**, 565–586 (2015). [arXiv:1503.05825](#) [nucl-ex]
55. CMS Collaboration, V. Khachatryan et al., Study of Z boson production in pPb collisions at $\sqrt{s_{NN}} = 5.02$ TeV. *Phys. Lett. B* **759**, 36–57 (2016). [arXiv:1512.06461](#) [hep-ex]
56. CMS Collaboration, A.M. Sirunyan et al., Observation of nuclear modifications in W^\pm boson production in pPb collisions at $\sqrt{s_{NN}} = 8.16$ TeV. *Phys. Lett. B* **800**, 135048 (2020). [arXiv:1905.01486](#) [hep-ex]
57. ALICE Collaboration, J. Adam et al., W and Z boson production in p-Pb collisions at $\sqrt{s_{NN}} = 5.02$ TeV. *JHEP* **02**, 077 (2017). [arXiv:1611.03002](#) [nucl-ex]
58. ALICE Collaboration, K. Senosi, Measurement of W-boson production in p-Pb collisions at the LHC with ALICE. PoS Bormio2015 042 (2015). [arXiv:1511.06398](#) [hep-ex]
59. LHCb Collaboration, R. Aaij et al., Observation of Z production in proton-lead collisions at LHCb. *JHEP* **09**, 030 (2014). [arXiv:1406.2885](#) [hep-ex]
60. ALICE Collaboration, S. Acharya et al., Z-boson production in p-Pb collisions at $\sqrt{s_{NN}} = 8.16$ TeV and Pb-Pb collisions at $\sqrt{s_{NN}} = 5.02$ TeV. [arXiv:2005.11126](#) [nucl-ex]
61. J.M. Campbell, R.K. Ellis, C. Williams, Vector boson pair production at the LHC. *JHEP* **07**, 018 (2011). [arXiv:1105.0020](#) [hep-ph]
62. M. Walt, I. Helenius, W. Vogelsang, A QCD analysis for nuclear PDFs at NNLO. PoS DIS2019 039 (2019). [arXiv:1908.04983](#) [hep-ph]
63. C. Anastasiou, L.J. Dixon, K. Melnikov, F. Petriello, High precision QCD at hadron colliders: Electroweak gauge boson rapidity distributions at NNLO. *Phys. Rev. D* **69**, 094008 (2004). [arXiv:hep-ph/0312266](#)
64. S. Alekhin, The NNLO predictions for the rates of the W / Z production in anti-p p collisions, in 21st International Symposium on Lepton and Photon Interactions at High Energies (LP03). 7, (2003). [arXiv:hep-ph/0307219](#)
65. PHENIX Collaboration, S.S. Adler et al., Centrality dependence of π^0 and eta production at large transverse momentum in $s(NN)^{1/2} = 200$ -GeV d+Au collisions. *Phys. Rev. Lett.* **98**, 172302 (2007). [arXiv:nucl-ex/0610036](#) [nucl-ex]
66. STAR Collaboration, B.I. Abelev et al., Inclusive π^0 , η , and direct photon production at high transverse momentum in p + p and d+Au collisions at $\sqrt{s_{NN}} = 200$ GeV. *Phys. Rev. C* **81**, 064904 (2010). [arXiv:0912.3838](#) [hep-ex]
67. D. de Florian, R. Sassot, P. Zurita, M. Stratmann, Global analysis of nuclear parton distributions. *Phys. Rev. D* **85**, 074028 (2012). [arXiv:1112.6324](#) [hep-ph]
68. J.F. Owens, J. Huston, C.E. Keppel, S. Kuhlmann, J.G. Morfin, F. Olness, J. Pumplin, D. Stump, The Impact of new neutrino DIS and Drell-Yan data on large-x parton distributions. *Phys. Rev. D* **75**, 054030 (2007). [arXiv:hep-ph/0702159](#) [HEP-PH]
69. *in preparation*. The nCTEQ Collaboration, nCTEQ PDFs including νN DIS processes
70. A. Kusina, J.-P. Lansberg, I. Schienbein, H.-S. Shao, Gluon shadowing in heavy-flavor production at the LHC. *Phys. Rev. Lett.* **121**(5), 052004 (2018). [arXiv:1712.07024](#) [hep-ph]
71. H. Lai, J. Huston, S. Kuhlmann, F.I. Olness, J.F. Owens, D. Soper, W. Tung, H. Weerts, Improved parton distributions from global analysis of recent deep inelastic scattering and inclusive jet data. *Phys. Rev. D* **55**, 1280–1296 (1997). [arXiv:hep-ph/9606399](#)
72. M. Hirai, S. Kumano, T.H. Nagai, Determination of nuclear parton distribution functions and their uncertainties in next-to-leading order. *Phys. Rev. C* **76**, 065207 (2007). [arXiv:0709.3038](#) [hep-ph]
73. K. Eskola, H. Paukkunen, C. Salgado, EPS09: a new generation of NLO and LO nuclear parton distribution functions. *JHEP* **04**, 065 (2009). [arXiv:0902.4154](#) [hep-ph]
74. M. Walt, I. Helenius, W. Vogelsang, Open-source QCD analysis of nuclear parton distribution functions at NLO and NNLO. *Phys. Rev. D* **100**(9), 096015 (2019). [arXiv:1908.03355](#) [hep-ph]
75. J. Binnewies, B.A. Kniehl, G. Kramer, Next-to-leading order fragmentation functions for pions and kaons. *Z. Phys. C* **65**, 471–480 (1995). [arXiv:hep-ph/9407347](#) [hep-ph]
76. F. Faura, S. Iranipour, E.R. Nocera, J. Rojo, M. Ubiali, The Strangest Proton? [arXiv:2009.00014](#) [hep-ph]
77. ATLAS Collaboration, F. Giuliani, Determination of proton parton distribution functions using ATLAS data, in 2019 European Physical Society Conference on High Energy Physics (EPS-HEP2019) Ghent, Belgium, July 10-17, 2019. (2019). [arXiv:1909.06702](#) [hep-ex]
78. Particle Data Group Collaboration, M. Tanabashi et al., Review of Particle Physics. *Phys. Rev. D* **98**(3), 030001 (2018)
79. G. D'Agostini, On the use of the covariance matrix to fit correlated data. *Nucl. Instrum. Meth. A* **346**, 306–311 (1994)
80. D. Stump, J. Pumplin, R. Brock, D. Casey, J. Huston, J. Kalk, H. Lai, W. Tung, Uncertainties of predictions from parton distribution functions. 1. The Lagrange multiplier method. *Phys. Rev. D* **65**, 014012 (2001). [arXiv:hep-ph/0101051](#)